Icarus **159**, 210–233 (2002)
doi:10.1006/icar.2002.6875

Long- and Short-Term Photometric Behavior of Comet Hyakutake (1996 B2)

David G. Schleicher

Lowell Observatory, 1400 W. Mars Hill Road, Flagstaff, Arizona 86001
E-mail: dgs@lowell.edu

and

David J. Osip

Massachusetts Institute of Technology, MIT Building 54-420, 77 Massachusetts Avenue, Cambridge, Massachusetts 02139

Received April 4, 2001; revised February 27, 2002

Narrowband filter photometry observations of Comet Hyakutake (1996 B2) were used to investigate this comet's short-term variability as well as its behavior for the apparition as a whole. Utilizing measurements obtained on a total of 13 nights between February 9, 1996, and April 14, 1996, we find that the heliocentric distance (r_H) dependence of the production rates of OH and NH were much shallower than those for either the carbon-bearing species or the visible dust. Based on the OH measurements, the derived water r_H-dependence was also significantly less steep than expected from a basic water vaporization model and required an effective active surface area of about 29 km^2 at $r_H = 1.8$ AU, 16 km^2 at $r_H = 1$ AU, and only 13 km^2 at $r_H = 0.6$ AU. This decrease in active area may be due to seasonally induced variations of a heterogeneous surface, or due to a decreasing contribution of gas from icy grains in the innermost coma. The relative abundances of the minor gas species place Hyakutake into the "typical" category of comets in the A'Hearn *et al.* (1995, *Icarus* 118, 223–270) taxonomic classification system. The spectrum is generally redder at shorter wavelengths throughout the apparition; however, the dust color progressively changes from being significantly reddened (37%/1000 Å) at large r_H to near-solar at small r_H. This change of color with distance implies a significant change in grain sizes or a changing proportion between two or more grain populations.

A major outburst was initiated near March 19.9, just prior to the comet's close approach to Earth. The characteristic recovery from the outburst differed among the observed species, with OH recovering most rapidly, essentially returning to its baseline values by March 25. The spatial radial fall-off of OH throughout this interval was consistent with the expected nominal spatial distribution, while CN and C_2 displayed fall-offs consistent with a distributed source, and the dust fall-off was significantly less steep than $1/\rho$, possibly due to fragmenting grains. Rotational lightcurve amplitudes were largest for the OH, NH, and dust, again consistent with the carbon-bearing species primarily originating from a distributed source. Significant variations were observed in the lightcurve amplitude and phase shifts as functions of aperture size. Finally, a refined value for the rotation period of 0.2614 ± 0.0003 day was determined. © 2002 Elsevier Science (USA)

Key Words: **Hyakutake; comets; photometry; composition; rotation.**

Color versions of all figures are available on IDEAL (http://www.idealibrary.com).

I. INTRODUCTION

The close approach of Comet Hyakutake (C/1996 B2) in early 1996 provided a unique opportunity to investigate the innermost coma of a relatively bright, long period comet. A variety of "first detections" were made due to the observational circumstances combined with improved or new instrumentation by Lis *et al.* (1997), Matthews *et al.* (1996), Dutrey *et al.* (1996), Woodney *et al.* (1997), Bockelée-Morvan *et al.* (1998), Mumma *et al.* (1996), Brooke *et al.* (1996), and Lisse *et al.* (1996). Our own visible and near-UV observational campaign was primarily intended to search for rotational variability, to investigate innercoma morphology, and to intercompare this long-period comet with others observed over the course of our decades-long photometry program (cf. A'Hearn *et al.* 1995). Our initial analysis (Schleicher *et al.* 1998b) focused on determining Hyakutake's rotation period by utilizing dust measurements obtained in late March 1996. In that work, a well-constrained value for Hyakutake's period of 6.23 ± 0.03 h was only determined by the combined analysis of the photometric lightcurve and CCD imaging of the comet's innercoma morphology. These observations clearly showed that a strong puff or blob of material was released in the sunward direction each rotation, producing a single-peaked rotational lightcurve, while a much smaller secondary puff of material was also released, too weak to be detected in the lightcurve.

0019-1035/02 $35.00
© 2002 Elsevier Science (USA)
All rights reserved.

Here, we present analyses of our entire photometric data set, investigating the rotational variability of each of the measured gas species and further refining the rotation period previously determined. We also investigate the photometric nature of the strong outburst which occurred just prior to Hyakutake's close passage by Earth. Additionally, our results for the apparition as a whole are presented, including r_H-dependencies, derived minimum active area, and dust colors, providing an overall context in which to place the numerous observations of other investigators.

II. OBSERVATIONS AND REDUCTIONS

Observations

The observations reported here were obtained using conventional photoelectric photometers. A pulse counting system was used on the 31-inch (0.8-m) and the John S. Hall 42-inch (1.1-m) telescopes at Lowell Observatory, while a similar system, but using DC electronics, was used on the 24-inch (0.6-m) International Planetary Patrol telescope located at Perth Observatory. Both filter sets were part of the standard International Halley Watch (IHW) series of narrowband filters; these isolated emission features from OH, CN, C_2, and C_3, along with continuum positions at 3650 and 4845 Å. At Lowell, an additional non-IHW filter was used to isolate the NH band. Due to the relatively high extinction in the near-UV at low-elevation sites, neither OH nor NH was measured from Perth.

A typical measurement consisted of several 10–15-s integrations with each filter centered on the comet's apparent photocenter, along with similar sky integrations offset from the coma and tail. In some instances, when the comet was closest and brightest, observations were made in a series of apertures in rapid succession. In these cases, total integration times per filter as brief as 10 s were used to minimize variability due to rotation. Conversely, when the comet was still relatively faint in February, integration times as long as 90 s were sometimes used to improve signal-to-noise. In addition, comet flux standard stars were observed each night to determine nightly extinction coefficients and instrumental corrections for each filter. These were applied to reduce the comet measurements to calibrated magnitudes above the atmosphere.

A total of 109 observational sets were obtained during the 13 successful nights of observing, encompassing a heliocentric distance range from 1.87 to 0.59 AU. All of the observations were obtained prior to perihelion, May 1, 1996 ($q = 0.23$ AU). Nightly observational parameters, such as the heliocentric and geocentric distances, are listed in Table I. Photometer entrance aperture sizes varied from 20 to 150 arcsec in diameter, while projected aperture radii ranged from about 700 to 36,000 km. The time (UT) and aperture size—both as a diameter in arcseconds and as the log of the projected radius in kilometers (ρ)—for each individual observation are listed in Table II.

Revised Filter Calibration and Reduction to Fluxes

While the IHW filter set we used at Lowell has maintained original transmission characteristics, the older NH filter has degraded, resulting in a slowly decreasing fractional transmission of the NH emission band (3360 Å) as compared to when the filter was constructed. To first approximation, our measurements indicate that the rate of degradation has been nearly constant with time; thus a single correction factor of 1.69 was applied

TABLE I
Observing Circumstances and Fluorescence Efficiencies for Comet Hyakutake (1996 B2)

UT Date	r_H (AU)	Δ (AU)	Phase Angle (°)	$\dot{r}_H$ (km s^{-1})	log L/N[a] (erg s^{-1} molecule^{-1}) OH	NH	CN	Teles[b]
Feb 9.50	1.872	1.508	31.7	−28.8	−14.524	−13.195	−12.531	L31
Feb 19.75	1.698	1.163	34.4	−30.1	−14.506	−13.152	−12.504	P24
Feb 25.45	1.597	0.971	35.8	−30.8	−14.496	−13.139	−12.479	L42
Mar 1.47	1.507	0.803	37.0	−31.6	−14.480	−13.130	−12.458	L31
Mar 18.72	1.177	0.241	37.0	−34.8	−14.463	−13.117	−12.479	P24
Mar 19.42	1.163	0.220	36.8	−35.0	−14.466	−13.117	−12.479	L42
Mar 23.34	1.082	0.120	42.3	−35.9	−14.476	−13.119	−12.475	L31
Mar 24.37	1.061	0.106	50.5	−36.2	−14.477	−13.120	−12.472	L31
Mar 25.14	1.045	0.102	59.5	−36.4	−14.477	−13.121	−12.470	L31
Mar 29.24	0.958	0.165	99.5	−37.5	−14.466	−13.128	−12.450	L42
Mar 30.19	0.937	0.191	103.4	−37.8	−14.461	−13.131	−12.443	L42
Apr 13.17	0.614	0.629	107.6	−42.5	−14.531	−13.210	−12.448	L42
Apr 14.15	0.590	0.661	106.6	−42.8	−14.544	−13.217	−12.457	L42

[a] Fluorescence efficiencies are for $r_H = 1$ AU and are scaled by r_H^{-2} in the reductions.
[b] Telescope ID: L42 = Lowell 42-inch (1.1-m); L31 = 31-inch (0.8-m); P24 = Perth 24-inch (0.6-m).

TABLE II
Photometric Fluxes and Production Rates for Comet Hyakutake (1996 B2)

UT Date	UT Time	log r_H (AU)	Aper Size (arcsec)	log ρ (km)	log Emission Band Flux (erg cm^{-2} s^{-1}) OH	NH	CN	C_3	C_2	log Cont. Flux (erg cm^{-2} s^{-1} Å^{-1}) UC	BC	log Q (molecule s^{-1}) OH	NH	CN	C_3	C_2	log $A(\theta)f\rho$ (cm) UC	BC	log Q H_2O
Feb 9	11.68	0.272	55.1	4.48	–10.14	–11.20	–10.54	–10.31	–10.47	–13.42	–12.92	28.64	26.48	26.07	25.60	26.15	2.90	3.17	28.64
Feb 9	11.97	0.272	55.1	4.48	–10.13	–11.17	–10.54	–10.37	–10.46	–13.36	–12.95	28.65	26.51	26.07	25.55	26.16	2.97	3.14	28.65
Feb 9	12.31	0.272	55.1	4.48	–10.09	–11.07	–10.53	–10.34	–10.43	–13.41	–12.98	28.68	26.61	26.07	25.57	26.19	2.92	3.11	28.68
Feb 19	17.57	0.230	77.8	4.52	—	—	–10.05	—	–10.03	—	–12.51	—	—	26.13	—	26.18	—	3.23	—
Feb 19	17.70	0.230	54.6	4.36	—	—	–10.32	–10.06	–10.27	–12.97	–12.62	—	—	26.08	25.66	26.18	3.16	3.28	—
Feb 19	18.51	0.230	77.8	4.52	—	—	–10.05	—	–10.04	—	–12.52	—	—	26.12	—	26.17	—	3.22	—
Feb 25	10.16	0.203	53.4	4.27	–9.76	–10.67	–10.25	–9.96	–10.07	–12.76	–12.42	28.71	26.68	26.02	25.64	26.27	3.25	3.36	28.74
Feb 25	10.40	0.203	75.2	4.42	–9.54	–10.44	–10.02	–9.77	–9.84	–12.69	–12.31	28.70	26.67	26.03	25.68	26.28	3.17	3.32	28.73
Feb 25	10.67	0.203	26.5	3.97	–10.27	–11.08	–10.75	–10.33	–10.63	–13.07	–12.68	28.70	26.79	26.00	25.63	26.20	3.25	3.40	28.73
Feb 25	11.16	0.203	37.8	4.12	–10.03	–10.92	–10.50	–10.15	–10.35	–12.92	–12.55	28.69	26.68	26.01	25.62	26.22	3.24	3.38	28.72
Feb 25	11.40	0.203	75.2	4.42	–9.53	–10.46	–10.04	–9.78	–9.83	–12.67	–12.31	28.71	26.64	26.02	25.67	26.28	3.19	3.32	28.74
Mar 1	10.20	0.178	55.1	4.21	–9.60	–10.52	–10.05	–9.78	–9.87	–12.54	–12.19	28.72	26.69	26.07	25.68	26.34	3.32	3.44	28.76
Mar 1	10.49	0.178	55.1	4.21	–9.61	–10.49	–10.04	–9.77	–9.87	–12.57	–12.19	28.71	26.72	26.08	25.69	26.33	3.29	3.44	28.75
Mar 1	11.25	0.178	55.1	4.21	–9.58	–10.42	–10.04	–9.74	–9.88	–12.56	–12.18	28.74	26.79	26.07	25.71	26.32	3.31	3.45	28.78
Mar 1	11.97	0.178	109.7	4.50	–9.07	–9.99	–9.57	–9.42	–9.36	–12.30	–11.94	28.78	26.73	26.10	25.76	26.39	3.27	3.39	28.82
Mar 1	12.16	0.178	55.1	4.21	–9.57	–10.43	–10.04	–9.75	–9.86	–12.54	–12.17	28.75	26.78	26.08	25.71	26.34	3.33	3.46	28.79
Mar 18	15.44	0.071	38.8	3.53	—	—	–9.49	–9.32	–9.50	–11.68	–11.36	—	—	26.35	25.68	26.41	3.60	3.69	—
Mar 18	15.59	0.071	38.8	3.53	—	—	–9.50	–9.21	–9.50	–11.67	–11.35	—	—	26.33	25.79	26.41	3.61	3.70	—
Mar 18	15.78	0.071	54.6	3.68	—	—	–9.24	–9.03	–9.24	–11.54	–11.20	—	—	26.35	25.75	26.42	3.60	3.70	—
Mar 18	15.95	0.071	54.6	3.68	—	—	–9.24	–9.06	–9.23	–11.52	–11.21	—	—	26.35	25.73	26.43	3.62	3.69	—
Mar 18	18.89	0.071	38.8	3.53	—	—	–9.50	–9.25	–9.51	–11.64	–11.34	—	—	26.33	25.74	26.40	3.64	3.71	—
Mar 19	8.25	0.066	37.5	3.48	–9.20	–10.10	–9.58	–9.15	–9.42	–11.66	–11.31	28.83	26.84	26.25	25.82	26.48	3.59	3.70	28.93
Mar 19	8.47	0.066	149.9	4.08	–8.20	–9.17	–8.57	–8.36	–8.36	–11.06	–10.72	28.83	26.74	26.30	25.87	26.57	3.59	3.69	28.93
Mar 19	8.57	0.066	52.8	3.62	–8.93	–9.88	–9.31	–8.94	–9.14	–11.49	–11.15	28.84	26.80	26.27	25.83	26.52	3.60	3.71	28.94
Mar 19	9.40	0.066	37.5	3.48	–9.18	–10.12	–9.59	–9.16	–9.41	–11.64	–11.30	28.85	26.82	26.25	25.82	26.50	3.60	3.71	28.95
Mar 19	9.60	0.066	149.9	4.08	–8.18	–9.17	–8.57	–8.35	–8.36	–11.05	–10.72	28.84	26.74	26.30	25.88	26.57	3.59	3.69	28.94
Mar 19	9.68	0.066	75.3	3.78	–8.67	–9.61	–9.06	–8.73	–8.87	–11.34	–11.00	28.84	26.80	26.28	25.83	26.53	3.60	3.71	28.94
Mar 19	9.89	0.066	37.5	3.48	–9.18	–10.02	–9.59	–9.14	–9.42	–11.64	–11.30	28.85	26.92	26.25	25.84	26.49	3.60	3.71	28.95
Mar 19	10.49	0.066	37.5	3.48	–9.18	–9.99	–9.58	–9.14	–9.41	–11.64	–11.30	28.85	26.95	26.25	25.84	26.50	3.61	3.71	28.95
Mar 19	10.69	0.066	149.9	4.08	–8.19	–9.09	–8.57	–8.35	–8.36	–11.04	–10.71	28.83	26.83	26.30	25.88	26.57	3.60	3.69	28.93
Mar 19	10.77	0.066	75.3	3.78	–8.68	–9.52	–9.05	–8.73	–8.87	–11.33	–11.00	28.83	26.90	26.28	25.84	26.53	3.61	3.71	28.93
Mar 19	10.96	0.066	37.5	3.48	–9.18	–9.95	–9.58	–9.13	–9.42	–11.64	–11.29	28.85	26.99	26.26	25.85	26.49	3.60	3.72	28.95
Mar 19	11.79	0.066	37.5	3.48	–9.19	–9.96	–9.58	–9.13	–9.40	–11.65	–11.31	28.83	26.98	26.26	25.85	26.51	3.59	3.71	28.93
Mar 23	5.49	0.034	109.7	3.68	–7.93	–8.74	–8.22	–7.92	–8.00	–10.62	–10.29	29.13	27.21	26.64	26.17	26.93	3.83	3.92	29.25
Mar 23	5.77	0.034	77.9	3.53	–8.16	–8.96	–8.46	–8.11	–8.26	–10.77	–10.44	29.15	27.25	26.64	26.17	26.93	3.83	3.92	29.27
Mar 23	5.84	0.034	55.1	3.38	–8.41	–9.21	–8.73	–8.34	–8.54	–10.95	–10.61	29.16	27.27	26.62	26.16	26.90	3.80	3.91	29.28
Mar 23	5.91	0.034	38.7	3.23	–8.67	–9.48	–8.99	–8.54	–8.80	–11.12	–10.77	29.16	27.27	26.63	26.19	26.90	3.79	3.90	29.28
Mar 23	5.98	0.034	27.5	3.08	–8.96	–9.77	–9.38	–8.83	–9.14	–11.33	–11.02	29.14	27.24	26.50	26.13	26.82	3.73	3.80	29.26
Mar 23	6.07	0.034	19.6	2.93	–9.25	–10.14	–9.60	–9.12	–9.43	–11.52	–11.16	29.11	27.14	26.54	26.08	26.79	3.68	3.81	29.23
Mar 23	6.73	0.034	109.7	3.68	–7.88	–8.72	–8.20	–7.91	–7.98	–10.60	–10.29	29.18	27.24	26.66	26.18	26.95	3.85	3.93	29.30
Mar 23	6.79	0.034	19.6	2.93	–9.21	–9.94	–9.58	–9.07	–9.37	–11.47	–11.14	29.15	27.33	26.55	26.12	26.85	3.73	3.82	29.27
Mar 23	7.01	0.034	27.5	3.08	–8.92	–9.69	–9.29	–8.78	–9.11	–11.28	–10.94	29.18	27.32	26.59	26.18	26.85	3.77	3.88	29.30
Mar 23	7.93	0.034	27.5	3.08	–8.92	–9.67	–9.28	–8.76	–9.12	–11.26	–10.91	29.18	27.35	26.60	26.20	26.84	3.79	3.91	29.30
Mar 23	8.54	0.034	27.5	3.08	–8.90	–9.69	–9.28	–8.79	–9.11	–11.24	–10.90	29.19	27.32	26.60	26.17	26.85	3.82	3.92	29.31
Mar 23	8.99	0.034	27.5	3.08	–8.90	–9.64	–9.28	–8.75	–9.11	–11.24	–10.89	29.20	27.37	26.59	26.21	26.85	3.82	3.93	29.32
Mar 23	10.01	0.034	27.5	3.08	–8.89	–9.59	–9.28	–8.78	–9.12	–11.26	–10.91	29.21	27.42	26.60	26.18	26.85	3.79	3.91	29.33
Mar 23	10.08	0.034	109.7	3.68	–7.85	–8.71	–8.19	–7.90	–7.98	–10.59	–10.28	29.21	27.25	26.67	26.19	26.96	3.87	3.94	29.33
Mar 23	10.12	0.034	77.9	3.53	–8.10	–8.93	–8.44	–8.10	–8.24	–10.74	–10.42	29.21	27.28	26.66	26.19	26.95	3.86	3.94	29.33
Mar 23	10.16	0.034	55.1	3.38	–8.36	–9.15	–8.71	–8.31	–8.52	–10.91	–10.58	29.21	27.32	26.65	26.19	26.92	3.84	3.94	29.33
Mar 23	10.38	0.034	38.7	3.23	–8.61	–9.41	–8.97	–8.53	–8.79	–11.07	–10.75	29.22	27.34	26.65	26.20	26.92	3.83	3.92	29.34
Mar 23	10.44	0.034	27.5	3.08	–8.89	–9.66	–9.27	–8.78	–9.09	–11.26	–10.92	29.21	27.35	26.60	26.18	26.87	3.80	3.90	29.33
Mar 23	10.50	0.034	19.6	2.93	–9.19	–9.93	–9.57	–9.06	–9.41	–11.46	–11.12	29.17	27.35	26.57	26.14	26.81	3.74	3.84	29.29
Mar 23	11.01	0.034	27.5	3.08	–8.90	–9.68	–9.28	–8.79	–9.10	–11.29	–10.95	29.19	27.33	26.60	26.17	26.86	3.77	3.87	29.31
Mar 23	11.75	0.034	27.5	3.08	–8.92	–9.72	–9.28	–8.79	–9.10	–11.31	–10.97	29.18	27.30	26.60	26.17	26.86	3.74	3.85	29.30

TABLE II—*Continued*

UT Date	UT Time	log r_H (AU)	Aper Size (arcsec)	log ρ (km)	log Emission Band Flux (erg cm^{-2} s^{-1}) OH	NH	CN	C_3	C_2	log Cont. Flux (erg cm^{-2} s^{-1} Å^{-1}) UC	BC	log Q (molecule s^{-1}) OH	NH	CN	C_3	C_2	log $A(\theta)f\rho$ (cm) UC	BC	log Q H_2O
Mar 24	5.23	0.026	109.7	3.62	–7.98	–8.73	–8.20	–7.89	–7.97	–10.64	–10.30	29.03	27.18	26.61	26.14	26.91	3.74	3.85	29.15
Mar 24	6.89	0.026	38.7	3.17	–8.63	–9.48	–8.97	–8.54	–8.78	–11.15	–10.81	29.17	27.22	26.60	26.13	26.88	3.69	3.79	29.29
Mar 24	6.97	0.026	109.7	3.62	–7.85	–8.74	–8.17	–7.88	–7.96	–10.63	–10.30	29.16	27.17	26.64	26.15	26.93	3.75	3.84	29.28
Mar 24	7.05	0.026	77.9	3.48	–8.10	–8.97	–8.43	–8.09	–8.23	–10.80	–10.47	29.16	27.19	26.63	26.14	26.91	3.74	3.83	29.28
Mar 24	7.13	0.026	55.1	3.33	–8.37	–9.23	–8.70	–8.31	–8.51	–10.98	–10.64	29.16	27.20	26.61	26.13	26.89	3.70	3.80	29.28
Mar 24	7.18	0.026	38.7	3.17	–8.62	–9.48	–8.97	–8.55	–8.78	–11.16	–10.82	29.18	27.23	26.60	26.13	26.88	3.67	3.78	29.30
Mar 24	7.25	0.026	27.5	3.02	–8.91	–9.77	–9.26	–8.81	–9.09	–11.34	–10.99	29.14	27.20	26.57	26.10	26.83	3.65	3.76	29.26
Mar 24	7.36	0.026	19.6	2.88	–9.20	–9.98	–9.57	–9.06	–9.82	–11.55	–11.18	29.12	27.26	26.53	26.09	26.36	3.58	3.71	29.24
Mar 24	7.67	0.026	27.5	3.02	–8.90	–9.70	–9.25	–8.78	–9.22	–11.35	–11.00	29.16	27.27	26.58	26.13	26.70	3.64	3.75	29.28
Mar 24	8.60	0.026	27.5	3.02	–8.87	–9.74	–9.25	–8.80	–9.21	–11.30	–10.96	29.18	27.23	26.58	26.11	26.71	3.69	3.79	29.30
Mar 24	9.00	0.026	109.7	3.62	–7.81	–8.76	–8.17	–7.88	–7.93	–10.63	–10.31	29.20	27.15	26.64	26.15	26.96	3.76	3.84	29.32
Mar 24	9.05	0.026	77.9	3.48	–8.07	–8.99	–8.43	–8.09	–8.21	–10.79	–10.47	29.19	27.18	26.63	26.14	26.92	3.74	3.83	29.31
Mar 24	9.09	0.026	55.1	3.33	–8.33	–9.23	–8.69	–8.31	–8.50	–10.95	–10.63	29.19	27.20	26.62	26.13	26.89	3.73	3.82	29.31
Mar 24	9.16	0.026	38.7	3.17	–8.59	–9.46	–8.97	–8.53	–8.82	–11.11	–10.77	29.20	27.25	26.61	26.14	26.84	3.73	3.83	29.32
Mar 24	9.23	0.026	27.5	3.02	–8.87	–9.64	–9.25	–8.77	–9.25	–11.28	–10.93	29.19	27.33	26.58	26.14	26.67	3.71	3.82	29.31
Mar 24	9.30	0.026	19.6	2.88	–9.15	–10.07	–9.56	–9.10	–9.80	–11.45	–11.12	29.17	27.16	26.53	26.06	26.38	3.68	3.77	29.29
Mar 24	10.14	0.026	27.5	3.02	–8.86	–9.65	–9.25	–8.77	–9.20	–11.27	–10.93	29.20	27.32	26.59	26.14	26.72	3.71	3.82	29.32
Mar 24	10.18	0.026	27.5	3.02	–8.87	–9.71	–9.26	–8.78	–9.21	–11.25	–10.91	29.18	27.26	26.58	26.13	26.71	3.73	3.84	29.30
Mar 24	10.90	0.026	27.5	3.02	–8.85	–9.65	–9.24	–8.78	–9.22	–11.27	–10.92	29.21	27.32	26.59	26.13	26.70	3.71	3.83	29.33
Mar 24	11.39	0.026	27.5	3.02	–8.85	–9.70	–9.25	–8.77	–9.21	–11.30	–10.96	29.21	27.27	26.58	26.14	26.71	3.69	3.79	29.33
Mar 24	12.03	0.026	27.5	3.02	–8.85	–9.77	–9.26	–8.80	–9.16	–11.33	–10.99	29.20	27.21	26.58	26.11	26.75	3.65	3.76	29.32
Mar 24	12.38	0.026	27.5	3.02	–8.86	–9.74	–9.26	–8.79	–9.19	–11.34	–11.00	29.20	27.24	26.57	26.13	26.72	3.64	3.74	29.32
Mar 25	2.65	0.019	27.5	3.01	–9.10	–9.85	–9.28	–8.84	–9.11	–11.41	–11.03	28.93	27.09	26.52	26.04	26.78	3.54	3.68	29.05
Mar 25	2.77	0.019	109.7	3.61	–8.10	–8.82	–8.20	–7.90	–8.00	–10.72	–10.36	28.88	27.06	26.58	26.10	26.87	3.64	3.76	29.00
Mar 25	2.80	0.019	77.9	3.46	–8.32	–9.01	–8.45	–8.11	–8.25	–10.88	–10.52	28.91	27.13	26.58	26.09	26.86	3.63	3.75	29.03
Mar 25	2.84	0.019	55.1	3.31	–8.57	–9.24	–8.71	–8.33	–8.51	–11.04	–10.69	28.93	27.17	26.57	26.09	26.85	3.61	3.73	29.05
Mar 25	2.87	0.019	38.7	3.16	–8.82	–9.49	–8.98	–8.56	–8.79	–11.21	–10.85	28.94	27.18	26.56	26.09	26.84	3.60	3.72	29.06
Mar 25	2.91	0.019	27.5	3.01	–9.08	–9.75	–9.27	–8.81	–9.08	–11.38	–11.01	28.95	27.20	26.53	26.08	26.81	3.57	3.70	29.07
Mar 25	2.95	0.019	19.6	2.86	–9.34	–10.01	–9.58	–9.06	–9.40	–11.58	–11.19	28.95	27.20	26.48	26.06	26.75	3.53	3.68	29.07
Mar 25	3.05	0.019	19.6	2.86	–9.37	–10.05	–9.57	–9.07	–9.43	–11.54	–11.17	28.93	27.16	26.49	26.05	26.72	3.56	3.70	29.05
Mar 25	3.66	0.019	27.5	3.01	–9.03	–9.73	–9.28	–8.80	–9.08	–11.35	–10.99	29.00	27.22	26.53	26.08	26.81	3.60	3.73	29.12
Mar 25	4.10	0.019	27.5	3.01	–9.00	–9.75	–9.28	–8.84	–9.11	–11.30	–10.96	29.03	27.20	26.52	26.04	26.78	3.65	3.76	29.15
Mar 29	3.12	–0.019	37.5	3.35	–8.77	–9.61	–9.00	–8.65	–8.91	–11.24	–10.89	28.93	27.01	26.48	26.01	26.68	3.71	3.83	29.07
Mar 29	3.26	–0.019	149.9	3.95	–7.76	–8.71	–7.98	–7.86	–7.75	–10.64	–10.29	28.95	26.89	26.54	26.08	26.86	3.71	3.82	29.09
Mar 29	3.32	–0.019	75.3	3.65	–8.26	–9.13	–8.46	–8.22	–8.28	–10.96	–10.60	28.93	26.97	26.52	26.04	26.80	3.69	3.82	29.07
Mar 29	3.94	–0.019	37.5	3.35	–8.80	–9.65	–9.00	–8.67	–8.91	–11.29	–10.93	28.90	26.97	26.48	26.00	26.67	3.66	3.79	29.04
Mar 29	4.07	–0.019	149.9	3.95	–7.78	–8.70	–7.98	–7.86	–7.76	–10.65	–10.30	28.93	26.90	26.54	26.08	26.85	3.70	3.82	29.07
Mar 29	4.61	–0.019	37.5	3.35	–8.82	–9.64	–9.00	–8.69	–8.92	–11.28	–10.94	28.88	26.99	26.48	25.98	26.66	3.67	3.78	29.02
Mar 29	5.04	–0.019	37.5	3.35	–8.80	–9.65	–9.00	–8.68	–8.92	–11.29	–10.94	28.90	26.97	26.48	25.99	26.66	3.67	3.78	29.04
Mar 29	5.45	–0.019	37.5	3.35	–8.79	–9.62	–9.00	–8.67	–8.90	–11.29	–10.96	28.92	27.01	26.48	26.00	26.69	3.66	3.75	29.06
Mar 29	5.80	–0.019	37.5	3.35	–8.79	–9.56	–9.00	–8.67	–8.91	–11.31	–10.93	28.91	27.06	26.48	25.99	26.68	3.64	3.79	29.05
Mar 30	3.61	–0.028	37.5	3.41	–8.74	–9.59	–8.96	–8.64	–8.78	–11.27	–10.92	28.94	27.02	26.51	26.04	26.79	3.72	3.84	29.09
Mar 30	3.86	–0.028	149.9	4.02	–7.75	–8.67	–7.95	–7.87	–7.74	–10.63	–10.31	28.95	26.92	26.57	26.12	26.88	3.77	3.85	29.10
Mar 30	3.98	–0.028	37.5	3.41	–8.76	–9.59	–8.97	–8.65	–8.79	–11.29	–10.94	28.92	27.02	26.49	26.02	26.78	3.70	3.82	29.07
Mar 30	4.35	–0.028	75.3	3.72	–8.24	–9.09	–8.42	–8.24	–8.24	–10.95	–10.61	28.93	27.00	26.55	26.06	26.84	3.75	3.85	29.08
Mar 30	4.55	–0.028	37.5	3.41	–8.79	–9.61	–8.96	–8.67	–8.79	–11.26	–10.92	28.89	27.00	26.50	26.01	26.78	3.73	3.84	29.04
Mar 30	5.04	–0.028	37.5	3.41	–8.78	–9.60	–8.96	–8.68	–8.78	–11.29	–10.97	28.90	27.01	26.50	26.00	26.79	3.71	3.80	29.05
Mar 30	5.11	–0.028	37.5	3.41	–8.79	–9.61	–8.96	–8.68	–8.79	–11.29	–10.96	28.89	27.00	26.50	26.00	26.79	3.71	3.80	29.04
Mar 30	5.42	–0.028	37.5	3.41	—	–9.66	–8.97	–8.68	–8.79	–11.27	–10.94	—	26.95	26.49	26.00	26.79	3.72	3.82	—
Apr 13	4.09	–0.212	52.8	4.08	—	—	—	—	–7.73	—	–10.52	—	—	—	—	27.36	—	4.25	—
Apr 14	3.21	–0.229	37.5	3.95	–8.20	–9.00	–8.13	–8.32	–7.94	–10.95	–10.68	29.18	27.24	27.03	26.51	27.30	4.18	4.22	29.43
Apr 14	3.43	–0.229	52.8	4.10	–7.97	–8.76	–7.90	–8.20	–7.73	–10.79	–10.56	29.22	27.26	27.08	26.56	27.34	4.19	4.19	29.47
Apr 14	3.59	–0.229	149.9	4.56	–7.43	–8.30	–7.37	–8.00	–7.31	–10.40	–10.25	29.30	27.18	27.20	26.66	27.41	4.13	4.05	29.55
Apr 14	3.72	–0.229	52.8	4.10	—	–8.77	–7.91	–8.21	–7.73	–10.79	–10.56	—	27.25	27.08	26.55	27.34	4.19	4.19	—
Apr 14	3.90	–0.229	37.5	3.95	—	–9.00	–8.17	–8.35	–7.95	–10.96	–10.69	—	27.23	26.99	26.48	27.29	4.17	4.21	—

to the Hyakutake NH fluxes obtained during the relatively short nine-week interval of this paper's observations. Two filters, isolating CN and C_3, from the Perth IHW set have also degraded in recent years. Unfortunately, in at least the case of the CN filter, the degradation has accelerated with time and we have insufficient transmission measurements over the years to directly determine a correction based on measured transmission characteristics. Instead, we have determined an empirical correction factor, based on several sets of near-concurrent observations from both sites of Comet Hale–Bopp during 1996. (A comet, rather than standard stars, must be used to determine the fraction of the emission band being transmitted, as compared to the amount of continuum.) Hale–Bopp is appropriate for this use, rather than Hyakutake itself, as Hale–Bopp showed almost no night-to-night variability during 1996, and the effects due to its overall brightening with time can be determined and removed based on the measurements from each site in the other, non-degraded filters. Logarithmic correction factors of 0.20 ± 0.02 and 0.11 ± 0.06 for the Perth CN and C_3 filters, respectively, were determined and applied to the flux data presented here.

The specific procedures used in the reduction from calibrated filter magnitudes to absolute band fluxes are revised and supersede the methodology used in past papers. The old method, detailed in A'Hearn *et al.* (1995), removed contamination of the 4845 Å continuum filter by the wing of the C_2 band, but it did not remove contamination of the 3650 Å continuum filter by the long blueward wing of the C_3 band, thus preventing dust colors from being properly investigated in gassy comets. For the new Hale–Bopp narrowband filter sets (cf. Farnham *et al.* 2000), an improved methodology was created which removed these contaminations of the UV and green continuum filters. In addition, the contamination of the CN filter by the C_3 wing is removed. Because the C_3 wings are much more extensive—3300–4400 Å—than was known when the original IHW reduction coefficients were calculated, the computed fraction of the total C_3 band which is transmitted by the C_3 filter (γ) is also different. This change in the fraction is substantial due to the large increase in the total band flux when one now includes the very long wings. In principle, this change in the total band flux and the resulting γ could be directly compensated for by a corresponding change in the fluorescence efficiency of the total emission band, because the original value of 1×10^{-12} erg s^{-1} molecule^{-1} was not strongly constrained (A'Hearn 1982). However, more recent determinations of the oscillator strength of the C_3 band (cf. Rousselot *et al.* 2001) are very close to the value originally adopted by A'Hearn. Therefore, rather than altering the fluorescence efficiency to force the same final abundances and production rates, we have, instead, kept the original value of 1×10^{-12} erg s^{-1} molecule^{-1} resulting in a large increase ($2.09\times$) in the derived C_3 abundance. A similar, but much smaller effect due to a change in the shape of the blueward wing occurs for C_2, resulting in a 10% increase in derived fluxes over the original IHW formulation. The derived NH and CN emission fluxes are slightly lower, 6 and 7% respectively, primarily due to a different absolute calibration of the standard stars in the near-UV.

The OH flux calibration is unchanged; however, a more robust method for determining the non-linear extinction for the OH filter near 3090 Å, where ozone is a major component of the total extinction, has been developed (Farnham *et al.* 2000). These new procedures have now been backapplied to the IHW filter set by Farnham and Schleicher (unpublished), and these improved reductions were utilized for the data presented here. During the backapplication process, a problem was discovered with the previous 4845-Å continuum filter absolute calibration coefficient, due to the presence of Hβ within this filter's bandpass coupled with the relative strength of this feature in our flux standard stars. Correcting this calibration coefficient results in a decrease by about 10% in derived filter fluxes for comets at 4845 Å. Derived continuum fluxes and resulting $A(\theta)f\rho$ values correspondingly decrease by 10% or more, depending on the gas-to-dust ratio and the proportion of 4845 Å flux due to C_2 contamination. Finally, this change for the 4845 Å continuum also propagates through to the continuum subtraction for each of the gas species, but for Hyakutake this effect is generally less than a few percent in the resulting gas fluxes. The resulting absolute continuum and emission band fluxes for the comet are tabulated in Table II. Further details of the new calibration procedures and the reduction coefficients will be presented in a future paper.

Calculation of Gas and Dust Production Rates

Standard procedures and coefficients (cf. A'Hearn *et al.* 1995) were used to further reduce the absolute emission band fluxes to abundances and then to production rates, and the continuum fluxes to $A(\theta)f\rho$, a measure of the dust production introduced by A'Hearn *et al.* (1984). Specifically, fluorescence efficiencies (L/N or, equivalently, g-factors) are applied for each molecular species to convert from band fluxes to the number of molecules present within the column defined by the photometer entrance aperture. For the diatomic molecules, the fluorescence efficiencies strongly vary with heliocentric velocity and, in the case of CN, also with heliocentric distance due to the Swings effect. These values are also presented in Table I. The Haser model (Haser 1957) was then used to extrapolate to a total number of molecules in the entire coma, and this value was divided by the assumed lifetime for the observed species to compute the production rate (Q). As discussed in previous papers (cf. Schleicher *et al.* 1998a, A'Hearn *et al.* 1995), to facilitate intercomparisons among the different gas species, we use the Haser model and Haser scalelengths having an r_H-squared dependence to reduce all molecular measurements. The dust production parameter $A(\theta)f\rho$—the product of the grain albedo at a particular phase angle, the filling factor, and the projected aperture radius—is aperture-independent for dust following a canonical $1/\rho$ fall-off in spatial distribution, and wavelength-independent

when the dust grains are gray in color. The final production rates are presented in Table II.

As previously discussed in more detail for Comets Halley (Schleicher *et al.* 1990) and Hyakutake (Schleicher *et al.* 1998b), these formulations of Q and $A(\theta)f\rho$ essentially assume a near-constant rate of release of material, which was not the case in either object due to rotational variability. As before, we make use of these parameters because they provide a first-order compensation for different aperture sizes and work well when we investigate long-term trends, such as the heliocentric distance dependence. However, they should not be treated as direct measures of the instantaneous release of material from the surface of the nucleus. In general, the rotational lightcurve for either Q or $A(\theta)f\rho$ will have a smaller amplitude and a phase lag when compared to the (unmeasured) source function at the nucleus, due to dilution by older material still within the observed column. Consequently, the larger projected apertures show the least amount of rotational modulation. The larger apertures also contain a larger fraction of the whole-coma abundance of each species, and so less extrapolation is needed when the Haser model is applied to compute the total abundance. Finally, in the innermost coma, which for Hyakutake was sampled in late March, canonical Haser scalelengths may not adequately reproduce the spatial profiles of the observed species, especially in the cases of C_2 and NH, both of which are believed to originate from grandparent species. In this situation, any two-generation model, which approximates the combined grandparent and parent as an effective single generation directly giving rise to the observed daughter, will be insufficient. To minimize these complications, analyses of long-term trends in behavior such as r_H-dependence in Section III were restricted to measurements obtained with relatively large projected apertures.

Calculation of Water Production Rates

We generally do not compute parent (or grandparent) production rates because most of the observed species have multiple parents and/or grandparents. For OH, however, only one parent exists, H_2O, and the velocities and lifetimes for both parent and daughter are reasonably well determined, permitting us to compute water production rates. Cochran and Schleicher (1992) previously determined an empirical conversion between their vectorial model for water and the Haser model used here. As discussed in more detail in Schleicher *et al.* (1998a) and A'Hearn *et al.* (1995), the conversion—$Q(H_2O) = 1.361\ r_H^{-0.5}\ Q(\mathrm{OH, Haser})$—primarily incorporates an $r_H^{-0.5}$ dependence of the water outflow velocity, which does not directly appear in the Haser formulation, a branching ratio of 0.90 for water to OH, and the value of r_H at which the two models yield the same production rate.

Uncertainties

Because Hyakutake was quite bright for most of its apparition, uncertainties based on photon statistics are typically less than 1% of the absolute flux for all species other than NH, and even for this relatively weak emission band whose errors are dominated by continuum subtraction, the formal uncertainties are usually less than 3%. The primary exceptions occur on the first two nights of observations in February, for which the overall signal-to-noise ratio is lower than on all subsequent nights, and on the last night of observing where the high airmass (>3) of some observations strongly affected the quality of the OH measurements. Ultimately, we removed the two highest airmass OH points on April 14, and two ultraviolet continuum measurements (and the corresponding C_3 measurements) on February 19.

III. WHOLE APPARITION RESULTS

Heliocentric Distance Dependence

In Fig. 1 we display the production rates of each gas species and $A(\theta)f\rho$ at 4845 Å as a function of heliocentric distance (r_H) as log–log plots. Observations obtained at Lowell are represented as circles, while Perth data are given as triangles. As detailed below, measurements through large projected apertures are shown as filled symbols and smaller apertures are indicated with open symbols. Some overlapping points have been slightly offset in r_H to better distinguish the individual points. In addition to the basic trend with heliocentric distance, the most obvious characteristics are the presence of an outburst just beyond 1 AU and the relatively large dispersions within individual nights in late March due to rotational variability and aperture effects.

While the disentanglement of these superposed items ultimately proved to be the most difficult aspect of our analyses, the first step—determining and removing the trend with r_H for each species—was relatively straightforward. This is primarily because most of the dispersion from a simple linear trend in the data occurred near 1 AU, in the middle of the range of log r_H. Therefore, the derived slopes were only weakly influenced by the effects of aperture size, rotational variability, and the outburst. To further minimize these effects on the r_H-dependence estimation, we examined the consequences of restricting the range of aperture sizes. As previously noted in Section II, the amount of gas or dust measured in smaller entrance apertures is more susceptible to rotational variability and to inadequacies in the modeling of the radial distributions. In principle, the size of these effects depend on the outflow velocity and scalelengths of the species, both of which vary with r_H, and with the intrinsic time scale of variations in the rate of release of material from the nucleus, which is independent of r_H. For Hyakutake, testing this parameter space confirmed that the latter effect dominated and that a single constraint on aperture size could be used for the complete range in r_H. The particular value for this cut-off was determined empirically. Specifically, projected aperture radii of less than 5000 km showed strong rotational variations and/or aperture effects in all species, and NH continued to show significant aperture effects if apertures smaller than 6000 km were included. Excluding measurements from

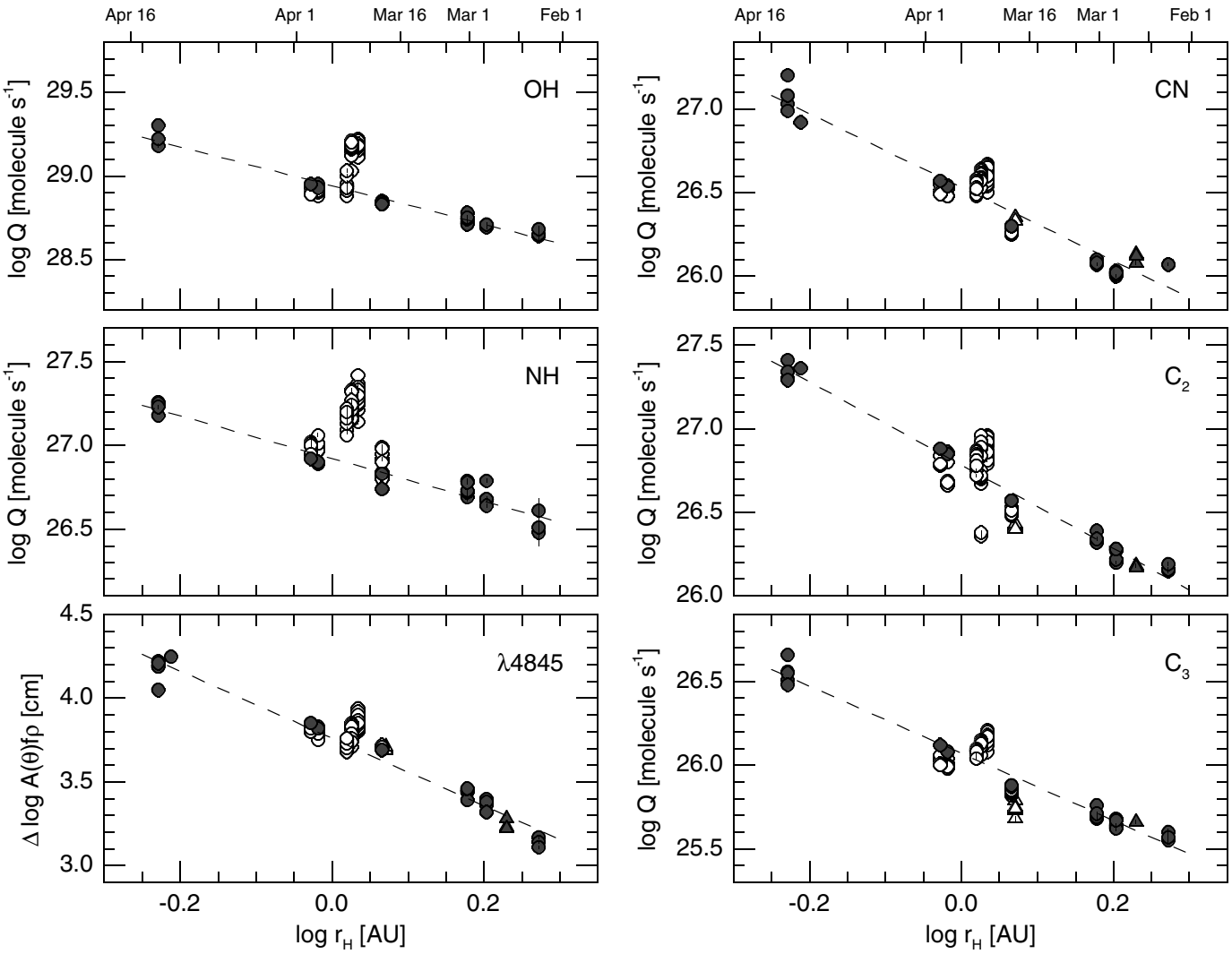

FIG. 1. Log of the production rates for each observed molecular species and $A(\theta)f\rho$ for the continuum at λ4845 plotted as a function of the log of the heliocentric distance. All observations were obtained prior to perihelion. Circles represent data obtained at Lowell Observatory and triangles are measurements taken at Perth Observatory. Filled symbols indicate large projected aperture measurements ($\rho > 8000$ km) used for the linear least-squares fit (see text) while smaller apertures are identified by open symbols. Note the significantly shallower slopes for OH and NH as compared to the other species, and the large apparent dispersion within many individual night's observations, due to rotational variability and aperture effects. An outburst lasting several nights is also evident just beyond 1 AU.

apertures smaller than 6000 km also conveniently removed all of the points associated with the major outburst, since no large ρ measurements were obtained near perigee due to the extreme spatial scales.

However, placing the cut-off much above 10,000 km excluded too many points at smaller heliocentric distances (<1 AU). Since there was also a gap in the aperture sizes used for Hyakutake between these possible values, we selected a value within the gap, 8000 km, as the best compromise of minimizing induced scatter but maximizing the number of data points included in our linear fits. The included points are shown as filled symbols in Fig. 1, along with the resulting unweighted linear least-squares fits. The slope of the fit for each species is presented in Table III. Note that the r_H-dependencies of OH and NH are much more shallow than those of the carbon-bearing species or the dust.

We are aware of only one other published Hyakutake data set with measurements of the same species in the visible portion of the spectrum and having sufficient temporal coverage to determine r_H-dependencies. Hicks and Fink (1997) observed Hyakutake spectra on nine nights between February 17 and April 17, and extracted production rate estimates for various gas species and continuum. From their data, they determined power-law slopes of approximately −2.5 for C_2 and −1.5 for water, CN, and $Af\rho$. However, they also report that haze was present on their last two nights, April 16 and April 17, allowing

TABLE III
Heliocentric Distance Dependences, Aperture Dependences, and Abundance Ratios for Comet Hyakutake (1996 B2)

Species	r_H– dependence	Aperture Fit Coefficients[a] A(0)	A(1)	A_{8000}	log Production Rate Ratios (X/OH)
OH	–1.18±.05	+0.0664	–0.0180	–0.0038	0.00
NH	–1.31±.07	+0.5543	–0.1711	–0.1130	–1.93±.09
CN	–2.22±.09	–0.2721	+0.0875	+0.0692	–2.53±.12
C_3	–1.99±.05	–0.0504	+0.0167	+0.0147	–2.98±.09
C_2	–2.46±.05	–0.4462	+0.1423	+0.1088	–2.29±.16
UC	–2.30±.07	–0.2903	+0.0927	+0.0712	–25.36±.13[b]
BC	–1.99±.06	–0.2007	+0.0639	+0.0485	–25.26±.12[b]

[a] Linear fits to the log of the projected aperture size; A_{8000} is offset to normalize to ρ=8000 km. See Figure 4.
[b] For ultraviolet and blue continuum, $A(\theta)f\rho$; ratio has units of cm sec mol^{-1}.

only upper limits to be estimated (see Fig. 4 from Hicks and Fink 1997). The different methodology of long slit spectroscopy versus aperture photometry, coupled with the use of different model scalelengths, makes it difficult to directly compare their derived slopes. However, we further explore the consistency between their data and ours for both water and dust production in the following sections. In the radio regime, several other minor species were measured systematically with time by Biver *et al.* (1999). These all showed linear trends in log–log space down to 0.57 AU before perihelion, and four of the five molecules—CO, CH_3OH, HCN, and H_2CO—have slopes of -2.2 ± 0.2, similar to what we measure for CN, C_2, and C_3. Their fifth species, CS, had a slope of -3.7 ± 0.4, which they note does not appear to be caused by their choice in model parameters.

As is evident from both the plots and Table III, OH and NH have much shallower r_H-dependencies than do any of the other molecular species or the dust. A shallower slope for OH has also been observed in other comets, most notably in 1P/Halley (Schleicher *et al.* 1998a) and 2P/Encke (A'Hearn *et al.* 1985; A'Hearn *et al.* 1995). In the former case, however, NH followed the carbon-bearing species, rather than OH. In contrast, the r_H-dependencies in Encke of both the NH and dust were better matched to OH than to the carbon-bearing species. In both comets, the variation in r_H-dependencies among the observed species was interpreted as evidence of heterogeneity within a rotating nucleus with different active source regions responsible for the primary emission through the apparition. As discussed further in subsequent sections, this seasonal scenario is consistent with Hyakutake's photometric behavior, while an alternative explanation would invoke an additional supply of icy grains which decreased with time.

Regarding the absolute slopes, rather than relative slopes among species, Hyakutake's r_H-dependencies are systematically less steep than for either Halley or Encke. Using the dynamical classification scheme of A'Hearn *et al.* (1995), Hyakutake would be designated as a young, long-period comet, due to its having a value of $1/a$ of 0.00105 AU^{-1}, where a is the semi-major axis. Within this class, Hyakutake's absolute r_H-dependencies are most similar to those of Comet Hartley–Good (1985 XVII = 1985 R1); however, the r_H-dependence of dust in Hartley–Good was even less steep than OH (A'Hearn *et al.* 1995). Note that Hartley–Good was also found to be the best match to Hyakutake in terms of polarization measurements (e.g., Kiselev and Velichko 1998).

Water Production

As expected, based on the empirical conversion factor noted in Section II, the power-law r_H-dependence of the vectorial equivalent absolute water production rates is 0.5 steeper than the value of the Haser Q(OH), yielding a slope of -1.68 (Fig. 2). (This does not nullify the previous intercomparisons of r_H-dependencies among species, since all of the daughter species were reduced to production rates in the same manner.) Our results for water are in very good agreement with Bertaux *et al.*'s (1998) water measurements based on Lyman-α measurements with SOHO, as well as the revised IUE values Bertaux *et al.* use in their Fig. 9 to extend the r_H coverage. And while they show a reasonable match to an r_H^{-2} slope, two of the three points plotted at larger r_H are artificially low because they are our Q(OH, Haser) points as published in an *IAU Circular* (Schleicher 1996) and were not converted to vectorial equivalent water production rates. Furthermore, the relatively high datum at small r_H from the April 16 SOHO measurement is associated with a strong outburst reported by Biver *et al.* (1999) and Hicks and Fink (1997). Correcting for both factors would yield a shallower r_H-dependence for water than the r_H^{-2} slope reported by Bertaux *et al.* We, therefore, conclude that our value for the r_H-dependence of water production of $r_H^{-1.68}$ provides a good measure of

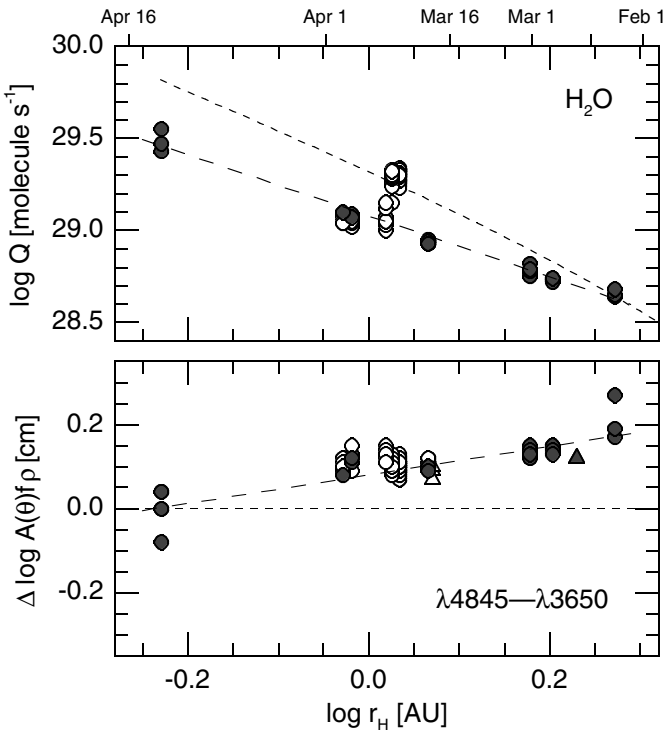

FIG. 2. Log of the water production rate (top) and dust colors (bottom) as a function of the log of r_H. Symbols are the same as in Fig. 1. Vectorial-equivalent water production rates are based on the Haser OH production rates (see text for details) and overlaid by a first-order fit to the large aperture data (filled symbols) having a slope of -1.68. The water production r_H-dependence is significantly less steep than would be expected from a basic water vaporization model (dashed curve). The color of the dust is shown as the differential log $A(\theta)f\rho$ for 4845 and 3650 Å.

Hyakutake's baseline behavior. This value is considerably shallower than the -2.32 that would be expected for a basic water vaporization model over this same range of r_H (0.6–1.9 AU) (based on Cowan and A'Hearn 1979), resulting in a decrease of the effective active area from about 29 km^2 near 1.8 AU to 16 km^2 at 1 AU, and only 13 km^2 at 0.6 AU. These values can be compared to the sustained active area of about 40 km^2 computed for 1P/Halley using the same model, a result in close agreement with spacecraft measurements (Schleicher *et al.* 1998a).

The simplest explanation of this change in effective area would be a seasonal effect, with the primary active region responsible for the rotational variations progressively receiving less solar radiation as "winter" approaches than would otherwise be the case. This scenario is consistent with the flattening of the production rates of numerous molecules observed in the radio regime at $r_H < 0.6$ AU and lower production rates after perihelion as compared to before (Biver *et al.* 1999). Alternatively, the change could be due to the eventual volatile depletion of a sustained icy-grain halo by sublimation and disintegration of the grains at smaller heliocentric distances. However, we show in Section IV that measurements of OH as a function of aperture size are only consistent with the presence of a significant icy-grain source if the water is released from the grains very close (<1000 km) to the nucleus.

Active Fraction of the Nucleus

We can also use the computed active area results to investigate the active fraction of the nucleus' surface and thus calculate a minimum nucleus radius. The largest minimum active area of 29 km^2 implies a minimum nucleus radius of 1.5 km assuming that 100% of the surface is active; at perigee, the derived area of 16 km^2 implies a minimum radius of 1.1 km. However, the large amplitude, single-peaked rotational lightcurve associated with the recurring puff or blob of material released each rotation at perigee (Schleicher *et al.* 1998b) clearly requires that this single, isolated active region is the source of a considerable fraction of the total outgassing. Thus, much of the surface must be much less active or even inactive, requiring a substantially larger nucleus radius than 1.1 km. The relative proportion of the entire outgassing which is caused by the primary active region is yet to be determined, but we hope to constrain this value in a subsequent, detailed analysis of our narrowband imaging data.

To estimate the percentage of the surface that is actively sublimating material, we can use the independent nuclear size estimates based on thermal, radio, and radar observations. Multiwavelength thermal imaging observations (Lisse *et al.* 1999) lead to an estimate of ~2.4 km for the nuclear radius of Hyakutake, while a smaller estimate of 2.1 km was found by Sarmecanic *et al.* (1996) using a more simplistic model of other IR measurements. The BIMA (de Pater *et al.* 1998) and VLA (Fernández *et al.* 1997) radio observations as well as the JCMT observations (Jewitt and Matthews 1997) provide consistent upper limits to the nuclear radius of between 2.4 and 3.0 km. Additional radio observations by Altenhoff *et al.* (1999) under admittedly adverse weather conditions lead to upper limits to the nucleus radius of between 1 and 4 km (assuming radio emmissivity of unity, cometary albedo of 0.03, and comet in temperature equilibrium). Finally, Harmon *et al.* (1997) estimate a smaller nuclear effective radius of 1.5 ± 0.5 km based on radar measurements. As noted by the authors, however, the radar observations estimate an equivalent radius of 2.5 km if the assumed radar albedo is lowered from 0.04 to 0.012 indicative of a very lightly packed material (also consistent with the reported break-off and outflow of nuclear surface chunks by Lecacheux *et al.* 1996 and others). An excellent discussion of the various nucleus size determinations can be found in Lisse *et al.* (1999) and Altenhoff *et al.* (1999).

If we adopt a value of approximately 2.4 km for Hyakutake's effective radius and ignore the possible contribution of icy grains, our vaporization modeling results would require approximately 40% of the nuclear surface to have been active at large r_H, and an active fraction of about 20–25% to produce the baseline water production at its closest approach to Earth in late March. This fractional active area is similar to that which was estimated for Comet Halley (Osip *et al.* 1992) but is much larger than the

active percentages determined for the majority of short-period comets (cf. A'Hearn *et al.* 1995). Note, however, that the method of accurately estimating nuclear sizes for these other comets was severely biased toward low activity comets.

Composition

As would be expected based on the relative r_H-dependencies of the observed gas species, the relative abundances or production rate ratios of CN, C_2, and C_3 remain essentially constant throughout Hyakutake's apparition, while each of these carbon-bearing molecules varied with respect to OH by large amounts. In particular, $Q(\mathrm{CN})/Q(\mathrm{OH})$ and $Q(\mathrm{C_2})/Q(\mathrm{OH})$ each increased by about a factor of 4 as Hyakutake approached the Sun. This behavior is similar to that observed in some other comets over a comparable range of r_H, most notably Comet Halley (Schleicher *et al.* 1998a, A'Hearn *et al.* 1995).

We can also compute the mean production rate ratio of each minor species to that of OH. For this, we have a choice of which data to include—i.e., either all points, only the large aperture measurements used for determining r_H-dependencies, or an intermediate selection such as all points except during the outburst. Ultimately, the final ratios were largely unaffected by the selection criteria, with only $Q(\mathrm{NH})/Q(\mathrm{OH})$ varying by as much as 30% primarily due to aperture effects. All other ratios varied less than 10%. Using an unweighted mean of all data, the log of the production rate ratios for the gas species were $\mathrm{CN/OH} = -2.53 \pm 0.12$, $\mathrm{C_2/OH} = -2.29 \pm 0.16$, $\mathrm{C_3/OH} = -2.98 \pm 0.09$, and $\mathrm{NH/OH} = -1.93 \pm 0.09$. The dust-to-gas ratios, as measured by log $A(\theta)f\rho/Q(\mathrm{OH})$ in units of cm s molecule^{-1}, were $\lambda 3650/\mathrm{OH} = -25.36 \pm 0.13$ and $\lambda 4845/\mathrm{OH} = -25.26 \pm 0.12$. These results can be compared to those of a "typical" comet, as defined by A'Hearn *et al.* (1995), but some cautions must be noted. Most important, as previously discussed in Section II, is the large change ($2.1\times$) in the derived C_3 total band fluxes due to the much more extensive wings of the emission band complex than was assumed in earlier reductions. Another, indirect effect, is the change in NH fluxes due to improved continuum removal. This would have little effect in dusty comets, but might substantially increase the derived NH fluxes in high gas-to-dust ratio objects in the A'Hearn *et al.* database. A future paper will investigate this issue in detail. At this time, we can only adjust the "typical" comet value of $Q(\mathrm{C_3})/Q(\mathrm{OH})$ upward by the constant value 0.32 in the log determined by the change in reduction coefficients. This results in a value of -3.27 ± 0.29, and a range of -3.94 to -2.77 for the "typical" comets in the A'Hearn *et al.* taxonomic classes and, with this adjustment to C_3, we can compare Hyakutake to the database results. The relative abundance of CN-to-OH in Hyakutake essentially matches the mean "typical" value, while C_2, C_3, and NH are all on the high side of the mean values but still well within the ranges defined as typical. This is not surprising, as A'Hearn *et al.* found that with a presumed Oort Cloud origin, nearly all long period comets are in this class. Finally, the ratio of dust-to-gas in this comet is relatively high, similar to that of P/Halley.

Dust Grains

The phase angle dependence of cometary dust grains is of great interest as it relates to grain properties, and a stronger than expected phase effect was observed for Halley at very small phase angles (Schleicher *et al.* 1998a). As a practical matter, because the phase angle depends on viewing geometry and often, therefore, varies with heliocentric distance, it can be difficult to separate out the phase effect. In the case of Hyakutake, due to its rapidly changing phase angle as it passed Earth, we had hoped to see clear evidence of variations due to phase. However, the range of phase angles Hyakutake went through (31.7°–106.6°) mostly coincided with the nearly flat portion of the phase function (Hanner and Newburn 1989, Gustafson and Kolokolova 1999). This, coupled with the several complicating behaviors, such as rotational variability and aperture effects, completely masked any phase effects that might have been present. Indeed, one might have expected an upturn in the apparent dust production at small r_H, when the comet's phase angle surpassed 90°, but the slight curvature evident from both continuum points is in the opposite sense. Because of the lack of any signature for a phase effect, we did not attempt to apply a correction as a function of phase angle to the derived $A(\theta)f\rho$ values.

Due to the new reduction procedures discussed in Section II, we can, for the first time, investigate possible trends in dust colors, without the added uncertainty of unknown gas contamination. Somewhat unexpectedly, a strong trend is seen with r_H, with the UV continuum at 3650 Å having a power-law slope 0.31 steeper than that of the blue continuum at 4845 Å, a difference much greater than the uncertainties in the slopes (see Table III). This trend, shown in Fig. 2, indicates that the color of the dust coma was becoming progressively more solarlike as the comet approached perihelion, from about 0.4 magnitude redder than solar (4845 Å : 3650 Å) or 37%/1000 Å at 1.9 AU, to essentially solar colors at 0.6 AU. Photometric colors on March 22, 1996, and March 23, 1996, by Lisse *et al.* (1999) using the IHW filters at 4845 and 6840 Å (0.11 magnitudes) complement our 4845 and 3650 Å (0.18 magnitudes) measurements, indicating that the continuum color was also more solarlike at longer wavelengths. To evaluate the persistence of this continuum color trend with r_H, we used $Af\rho$ values from Hicks and Fink (1997). Ignoring their upper-limit measurements of April 16–17 and removing the outburst observations of March 23–24, we extract an r_H-dependent continuum slope at 6250 Å of between -1.6 and -1.7. While significantly less steep than either of our continuum values, their continuum point at 6250 Å is considerably redward of our continuum points. In fact, a simple linear extrapolation with wavelength of the r_H-dependent continuum slopes reported above yields a slope of -1.67 at 6250 Å. To further investigate this trend with wavelength, we utilized the sample reflectance spectra shown by Hicks and Fink, and extracted continuum measurements at 8500 Å, a location clean of emission bands or telluric features. After scaling from their 6250 Å point, we derive a rough slope of -1.5 at 8500 Å, only somewhat less steep than the value at 6250 Å. Combining our

continuum colors with those from Hicks and Fink reveals that the dust color in the red (8500 Å : 6250 Å) is much more neutral than in the near-UV to visible at all distances, but again with the continuum being reddest early in the apparition and with the continuum rapidly becoming more solarlike in color as the comet approached perihelion. As a final check of these results, we look at photometric and polarimetric observations by Kiselev and Velichko (1998) using IHW filters at 3650, 4845, and 6840 Å. Their (4845 Å : 3650 Å) color excess of 0.17 magnitudes on April 5 at $r_H = 0.79$ AU is completely consistent with what would be predicted given our own color measurements and r_H dependencies. Furthermore, the (6840 Å : 4845 Å) colors and trends they observed between March 25 and April 5 are consistent with the data of Hicks and Fink and of Lisse *et al.* showing solar colors after April 11 at $r_H = 0.66$ AU.

In a detailed investigation of the properties of cometary dust from color and polarization measurements, Kolokolova *et al.* (1997) constructed a series of models based on various particle shapes and adopting particular indices of refraction and a range of individual particle size distribution functions. Their principal conclusion was that the dust color was most sensitively tied to the particle size distribution while the polarization was most strongly affected by the complex index of refraction (and thus the composition). Gustafson and Kolokolova (1999) and Kolokolova *et al.* (2001) have further combined theoretical modeling with laboratory microwave light scattering experiments to investigate the observable properties of aggregate structures that perhaps provide the closest analog to cometary dust particles (e.g., Greenberg and Gustafson 1981). They conclude that the observed color is redder when: (a) the size of the constituent particles is larger, (b) the imaginary index of refraction of the particles is larger, or (c) the aggregate is more compact. The specific particle shape was not found to have a significant effect on the aggregate color, although it did affect both the position and value of the maximum polarization.

The behavior of the continuum colors that we observe as a function of r_H clearly requires a change in some property of the grains with r_H. Since shape and compositional variations of the dust particles would manifest themselves in the polarization record, and no such variations are noted (Joshi *et al.* 1997, Kiselev and Velichko 1998, Manset and Bastien 2000), the most plausible explanation for the observed color changes would invoke either less compact aggregates or a different size distribution at smaller r_H. In the simplest terms, a redder color indicates that the ratio of large-to-small particles in the observed coma is greater than in a coma with nearly solar color. At high phase angles, one might expect that phase angle effects might contribute, but measurable phase effects have already been ruled out over the range of observed phase angles. Therefore, we believe the change with r_H is either due to a change in grain properties such as due to grain "fading," from grains darkening or shrinking or breaking apart with time (cf. Baum *et al.* 1992) or a changing proportion between two or more grain types.

As reported in Chernova *et al.* (1994) and noted in Kolokolova *et al.* (1997), Comet Shoemaker–Levy 1992 XIX showed a pronounced difference between the (3650 Å : 4845 Å) colors and the (4845 Å : 6840 Å) colors similar to what we report here. Since their data reduction did not account for possible C_3 contamination of the 3650 Å filter, the actual color difference could be even larger than they report and even closer to what we determine for Hyakutake. Kolokolova *et al.* were unable to resolve such a color trend as this with a change in a single size distribution for the coma particles and suggest two contributing size distributions of different power indices. We find this interpretation particularly attractive in the case of Hyakutake where two likely sources of the emission are proposed—one from the large active area responsible for the observed rotational variations and the other from a more widespread background source. If we follow our reasoning from the previous section regarding the decrease in the effective area for water production being due to seasonal effects of an active region going into winter or to a changing contribution from a near-nucleus icy grain population, we have two possible self-consistent pictures. In the first scenario, the major active source region is responsible for lifting either larger or more compact aggregates and, as the comet approaches the Sun, this region contributes a progressively smaller fraction of the total dust coma. In the alternative scenario, the change in grain populations would be due to either progressive devolatilizing of icy grains or to a decreasing supply of surface or subsurface grains to be lifted from the active source region.

IV. SHORT-TERM ACTIVITY RESULTS

To investigate short-term activity and aperture effects, we removed the r_H-dependent slopes from all observations of each species using the coefficients in Table III. The resulting values for $\Delta \log Q$ and $\Delta \log A(\theta) f\rho$ are shown as a function of time from perihelion (May 1.395) in Fig. 3 for the interval centered on perigee. Here the rotational variability and the outburst are clearly evident. Additional dispersion in the data is caused by aperture effects, which are identified by different symbols for different aperture sizes. Because our most complete temporal coverage occurred on the nights of March 23–25, the same nights as the outburst, we had to be exceptionally careful to cleanly separate the various components in the lightcurve. As noted previously, aperture effects are expected from rotational variability due to dilution by older material within the observed column, and the degree of dilution will increase with aperture size. Similarly, aperture effects might also be expected from an outburst originating from the nucleus; however, the behavior could be much different if the observed brightness enhancement was actually due to a piece of the nucleus breaking off and drifting away, as has been suggested by Lecacheux *et al.* (1996). Finally, we noted in Section II that standard two-generation Haser model scalelengths are unlikely to successfully reproduce the spatial profile of a granddaughter species very close to the nucleus, also resulting in possible trends with aperture size.

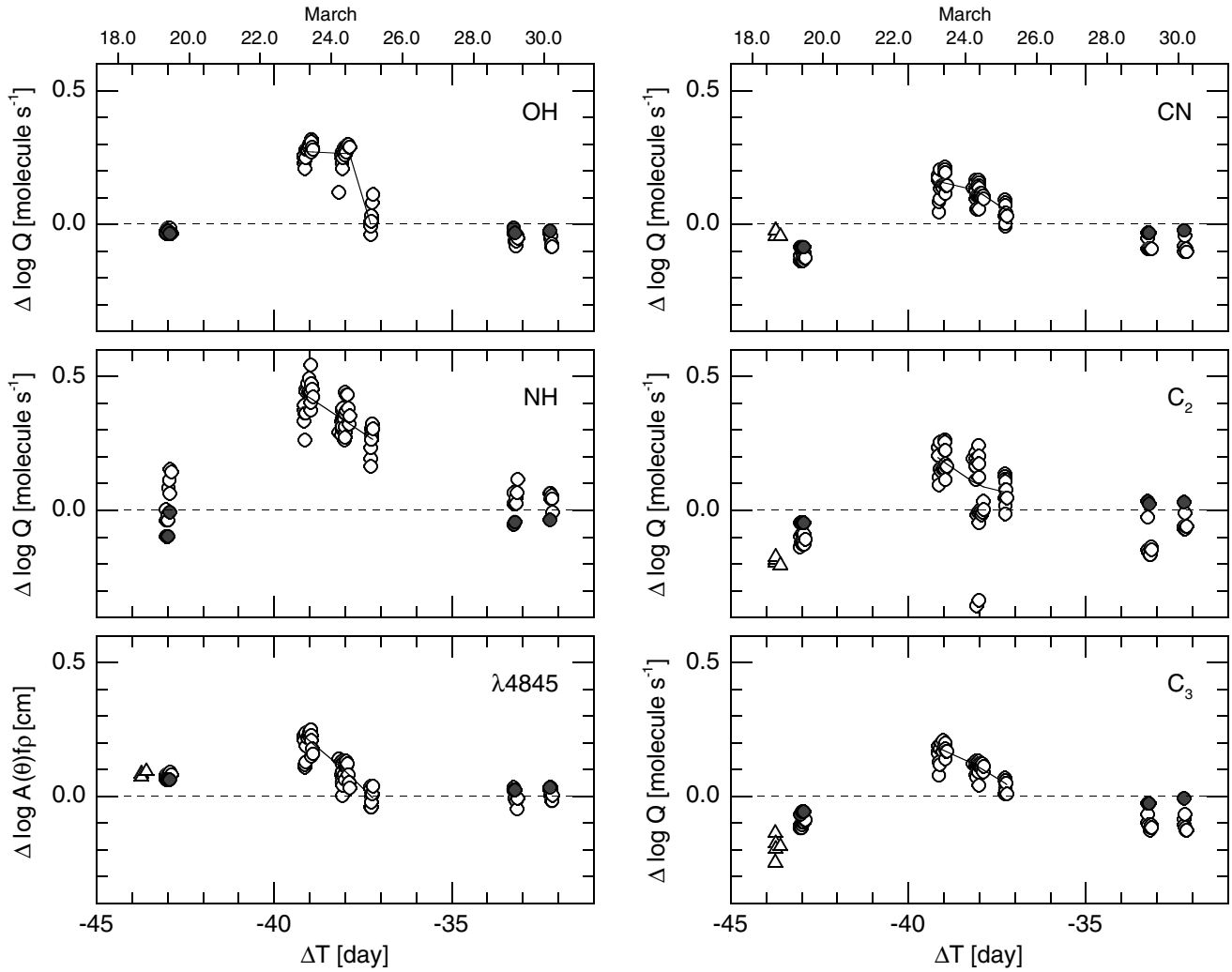

FIG. 3. Log of the production rates for each observed molecular species and $A(\theta)f\rho$ for the continuum at λ4845 plotted as a function of the time from perihelion (May 1.395) for late March, after removal of the r_H-dependent trends shown in Fig. 1. Symbols are the same as in Figs. 1 and 2. Again note the large apparent dispersion within the observations on individual nights due to rotational variability and aperture effects. The outburst which occurred just prior to perigee (March 25) is overlaid by the Lowess fits described in the text, which are removed during the first iteration to quantify aperture effects.

After considerable experimentation with different techniques applied in various orders to separate the observed lightcurve into these multiple components, we ultimately settled on a relatively simple iterative procedure. In brief, this involved first fitting the basic shape of the outburst on the nights of March 23–25 and removing it, and then using the residual values to determine the trend with aperture for each species. On the second iteration, these aperture trends were removed from all of the original values for $\Delta \log Q$ and $A(\theta)f\rho$, at which stage the outburst was recharacterized and again removed. The new residuals were rotationally phased to investigate rotational characteristics of each observed species, and, ultimately, to improve our previous determination of the rotation period. Fits to each species' rotationally phased data were used to remove the rotational variability in a final iteration, effectively leaving only the outburst for investigation. The appropriateness of the procedures employed at each stage will be discussed along with other details below.

First-Iteration Outburst Removal

The initial step in the separation process—the first-cut outburst removal—needed to address several specific characteristics of the data: The outburst began and apparently peaked prior to March 23, and the comet did not return to its baseline behavior until after the observations on March 25, but probably well before the next measurements on March 29 (see Fig. 3). In addition, the decay function varied considerably among the different gas species and the dust. For instance, as was shown in Schleicher *et al.* (1998b), the dust was adequately fit with a linear function on the three consecutive nights, whereas OH was at a comparable level on the first two nights and then dropped

sharply. The other gas species show fall-offs between these extremes, but generally more similar in shape to that of the dust grains. While the observations obtained within individual nights also provided clues as to the shape of the outburst as a function of time, ultimately there proved to be too few constraints to uniquely determine the complete shape. We, therefore, applied a smoothing function to give reasonable local baselines within each night. For this purpose, we chose the robust Lowess smoother (Cleveland 1979), which employs a single adjustable parameter, the "span," which controls the fraction of data that are included when the smoothed value for a particular datum is computed. Lowess smoothers have the advantage that they are good at determining general trends in data that are not necessarily spaced uniformly in time, but effectively ignore very short-term trends, such as caused by rotational variability, or individual discrepant points. The number of data points and their groupings influence the value of the span, and a span of 23% was found to work well for all of the species except OH when the entire data set (i.e., all 13 nights) was used as input; smaller or larger values for the span resulted in smoothed results for one or more species, which either followed the rotational variability or ignored night-to-night variations, respectively. For OH, the previously noted sharp drop-off between March 24 and March 25 results in a poor Lowess fit for both March 24 and March 25. A much better fit for March 24 was obtained using a simple linear regression through the data of March 23 and March 24, and this was used to remove the outburst on both nights. On March 25, OH had nearly returned to the overall baseline value, and so no adjustment to this night's data was applied.

Figure 3 shows these first-cut fits of the outburst, which were then removed for each species. Note that the Lowess function only computes a smoothed value for each datum, rather than true interpolated values of the independent variable, time. Therefore, the line segments connecting the points are not necessarily appropriate representations of intermediate values, especially for segments connecting one night to the next. This is not an issue in our iteration process since we are simply determining the adjustment required for each data point to remove the outburst.

Trends with Aperture Size

Having removed the first-cut fit to the outburst for each species, one can investigate the resulting residuals as a function of log ρ. As already noted in Section III, a wide range of relatively small-to-medium projected aperture radii (ρ) were measured in Hyakutake during its close approach to Earth. For the remainder of the apparition, observing windows were usually too short to obtain more than a couple of relatively large aperture measurements. To avoid possible systematics due to inexact r_H-dependence removals, possible minor outbursts, or rotational phase, we decided to only include data obtained at closest approach (March 23–25) in the primary analysis of aperture effects, using additional nights only to check these results. The resulting residuals as a function of log ρ are shown in Fig. 4, where the three different nights of observation are distinguished by different symbols. Strong trends with aperture size are present for NH, CN, C_2, and dust, with NH showing a significant decrease in its derived production rate with increasing aperture size while the dust and CN and C_2 display the opposite behavior. In addition, considerable scatter is present, primarily due to rotational variability. Because our priority was to obtain excellent rotational coverage using a monitoring aperture (27.5 arcsec diameter), full aperture sequences were measured on only five occasions but partial sequences were obtained on several additional occasions. Fortunately, these provided a good sampling of rotational phase, and so the trends with aperture size measured for each species are effectively averages over all rotational phases. Therefore, the fitted trends are robust measures of the bulk aperture effects, despite the considerable scatter. It was further confirmed that these trends were essentially independent of the outburst by examining the smaller range of aperture measurements on March 19, 29, and 30.

The specific trend with aperture size for each species was obtained by fitting using linear least squares. When the fits were determined, it became obvious that the smallest aperture points (19.6 arcsec) systematically fell below the respective trend lines for each species. We have, therefore, excluded these smallest aperture data when we determine the linear least-squares fits, since our purpose in fitting these trends is to apply the best empirical correction for aperture size to the data set as a whole; otherwise, the departures from a linear trend by the smallest aperture data would significantly bias the fits and yield poor extrapolations of the aperture trends to large apertures, which were only measured on other nights. Based both on three-sigma criteria and potential-residual plots, we also excluded from the fits a single abnormally low data point for both OH and CN. (One C_3 point, an NH point, and two C_2 data points were also abnormally low but were already excluded as they were obtained using the smallest aperture.) Finally, both OH and C_2 showed anomalous aperture behavior on single nights. In the case of C_2 on March 24, the smallest aperture points are very low (by 0.3 in the log), the numerous monitoring aperture (27.5 arcsec) points are somewhat low, while larger aperture measurements are systematically higher than corresponding values on both March 23 and March 25. While the two smallest aperture points would be eliminated by the exclusion criteria above, the overall aperture trend would still be significantly steeper on March 24 as compared to both March 23 and March 25. We have no ready explanation as to why the C_2 on March 24 is abnormal, as the two sets of aperture sequence measurements are at very different rotational phases. Since the aperture trends for C_2 on non-outburst nights have slopes consistent with March 23 and March 25, we only use March 23 and March 25 to determine the C_2 aperture fit. For OH on March 25, a significant downward trend with increasing aperture size is observed, unlike the nearly level fit which exists on all other nights, possibly caused by residual effects from the outburst. This night was therefore similarly excluded from the final fit with aperture size.

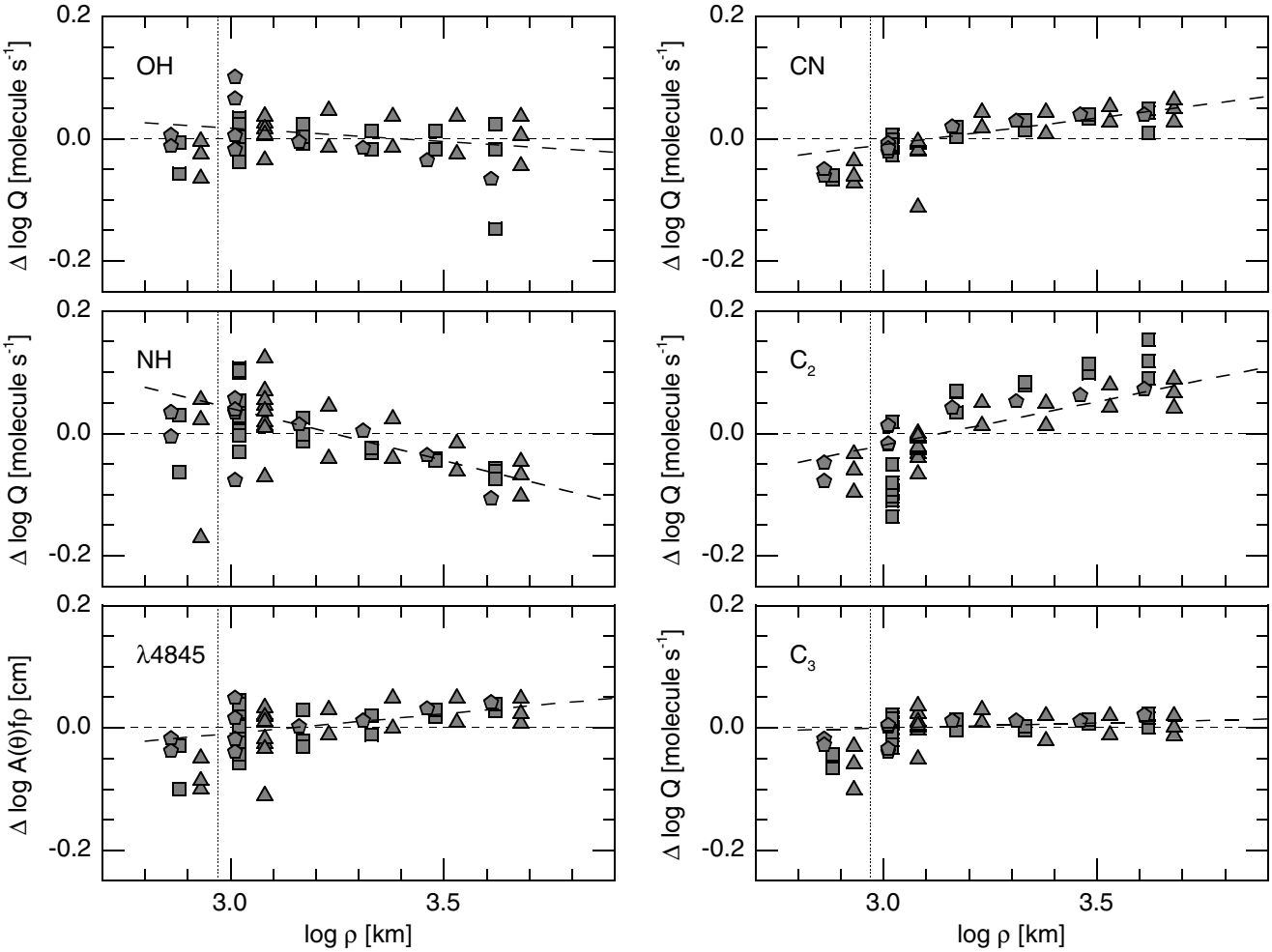

FIG. 4. Residual log of production rates for gas and dust plotted as a function of the log of the projected aperture radius (ρ) for March 23–25, after removal of the fits to the outburst shown in Fig. 3. Symbols distinguish the different nights, with triangles for March 23, squares for March 24, and pentagons for March 25. The linear least-squares fits to these trends with size were computed after the smallest aperture measurements to the left of the dotted vertical line were excluded because these data are systematically below the trends observed for the larger aperture data. Also excluded from the fits were the C_2 measurements from March 24, which displayed a much steeper trend with aperture size than on other nights, and OH from March 25, due to a larger than usual rotational amplitude. The coefficients of the fits are listed in Table III. The relatively large dispersion seen in OH, NH, and the dust is due to rotational variability.

The resulting linear fits are shown in Fig. 4. When attempting to decipher the cause of the individual aperture trends for each species, it is important to remember that these plots are not spatial profiles, but rather that each photometer entrance aperture also includes the material measured in the smaller apertures. Therefore, corresponding trends as a function of projected distance, rather than aperture size, would be even larger than those shown in Fig. 4. Since our overall trends are independent of rotation (being averages over rotational phase), they cannot be caused by short-term variability. They are also not induced by the outburst, since other nights' observations are consistent with the measured trends. Therefore, the most likely cause is due to our standard scalelengths being inappropriate for Comet Hyakutake. Since Hyakutake was observed at solar minimum, lifetimes will be longer than average, and our standard scalelengths might be expected to be correspondingly too short. Also, acceleration of gas and dust outflow velocities in the innermost coma will have an effect on the model spatial distributions. However, one would expect that if these factors controlled the observed trends, that all species would show similar trends. Since OH and C_3 show essentially no variation in derived Q as a function of aperture size, and NH is opposite of CN, C_2, and dust, we believe other effects dominate the variations among species, such as distributed sources. Indeed, the increasing values of $A(\theta)f\rho$ with aperture size require a spatial profile which is less steep than $1/\rho$, the reverse of what one obtains with accelerating grains. Instead this could be caused either by fragmenting grains, which increase the net surface area at visible wavelengths, or by large secondary chunks which have broken off from the nucleus (Desvoivres *et al.* 1999). For the carbon-bearing molecules, especially CN and C_2, it has often been proposed that the source of a significant fraction of the gas is from volatile grains

(cf. Laffont *et al.* 1998, Harris *et al.* 1997) such as CHON particles (Kissel *et al.* 1986), and either this or secondary "iceberg" sources could explain the aperture effects. In contrast, the flat aperture trends measured for OH and C_3 are consistent with these species' parents primarily being released directly from the nucleus or very near-nucleus region (<1000 km). Finally, we suspect that the decreasing trend of Q(NH) with aperture size is most likely due to its having the least well-determined scalelengths of any of these species (A'Hearn *et al.* 1995 and references therein).

Whatever the causes of these observed aperture effects, our primary goal in this paper is to empirically compensate for these trends so that other characteristics of the lightcurves can be investigated, such as rotational variability and the outburst. Accordingly, the linear fits shown in Fig. 4 and listed in Table III, with appropriate offsets applied to normalize the measurements to 8000 km ($\log \rho = 3.90$), have been used to adjust all data points subsequent to the r_H-dependence removal but prior to the first-cut outburst removal.

Second-Iteration Outburst Removal

Having adjusted the data for trends with aperture size, we next proceed to the second iteration, repeating the process of applying the Lowess smoothing function to determine the shape of the outburst as a function of time. Unlike the first iteration, here it is important what, if any, adjustment is made to data obtained on nights other than March 23–25. It became apparent that night-to-night variations from the baseline were too large to ignore, whether due to small outbursts or simply because the shape of the actual r_H-dependent behavior deviated somewhat from linear. Lowess smoothing again provided the most practical solution, and so we used nearly the same procedure that we employed in the first iteration, including the special treatment for the OH outburst. The only change is that a smaller value for the span parameter, 13%, was needed on nights other than March 23–25 to follow night-to-night variations, because far fewer observations were obtained on the non-outburst nights. Therefore, Lowess smoothing functions were fit to the entire data for each species twice, first using a 23% span to remove the outburst on March 23–25, and again using the 13% span to determine adjustments to be made for all other nights' data. Occasionally, this resulted in an overadjustment, because all of a particular night's observations were obtained near either a maximum or minimum in the rotational lightcurve. In these cases, we simply tracked these data points in the subsequent analyses, to avoid misinterpretation of these data. The smoothed values were removed from the data, again yielding residual production rates (ΔQ and $\Delta A(\theta) f\rho$), but now reflecting the underlying rotational variability of each species.

Rotational Variability

The rotational lightcurve characteristics can best be examined by rotationally phasing the observations. Phase plots for each species are shown in Fig. 5, where our improved rotation period of 6.2736 h (=0.26140 day) is used; this new period determination will be discussed in detail in the next section. Zero phase is defined at the time of perihelion, i.e., May 1.395. As would be expected, the amplitudes of the lightcurves vary among species and with projected aperture size. Also, substantial relative phase lags are also evident between species and with aperture size. Combined with these basic characteristics is the observational fact that systematically smaller apertures were observed on the nights of March 23–25, when the best rotational phase coverage was obtained. Therefore, we will display and discuss several different subsets of the data to simplify our examination of these data.

Our first look at the rotation lightcurves is presented in the left-hand column of Fig. 5, where we restrict the data points shown to those obtained with our 27.5 arcsec diameter monitoring aperture on March 23–25, for which ρ decreased from 1200 to 1020 km (see also Table IV). In these plots, the three nights' data are distinguished by different symbols. Immediately evident is that OH, NH, and the dust have clear, single-peaked lightcurves, while the carbon-bearing species show little or no rotational variation. Surprisingly, the granddaughter species NH has an amplitude somewhat larger than either that of the OH or dust (all range between 0.08 and 0.11 as measured by the Δ log of the production rate). In comparison, the species having the shortest lived parent and a short lifetime of its own, C_3, has only about one-half of this amplitude, when it normally exhibits the largest amplitude such as in Comets Halley (cf. Millis and Schleicher 1986, Schleicher *et al.* 1990) and Levy (1990c) (Schleicher *et al.* 1991).

While the observed differences in rotational amplitudes among species were not anticipated, they can be explained in retrospect. In the case of the dust, the amplitude is essentially determined by the outflow velocity, coupled with the rotation period and the aperture size. Therefore, the observed amplitude is expected to and does decrease with increasing aperture size due to increased dilution by older material still within the aperture. Because the time required for material to reach the edge of the aperture is comparable to the duration of activity, and both are small (about 1 h) compared to the rotation period, the amount of dilution is also fairly small. Three additional considerations apply to the daughter (or granddaughter) gas species. First, the bulk outflow velocity of the gas is higher than that of the dust, therefore the gas reaches the edge of the aperture more rapidly, resulting in larger amplitudes. Conversely, there can be substantial additional dilution caused by daughter molecules backflowing into the aperture, either due to the excess, random velocities imparted to the daughters after dissociation of parent molecules outside of the aperture or due to a distributed source outside of the aperture. In addition, species having longer lived parents generally show smaller amplitudes. The very fact that OH and NH display comparable amplitudes to that of the dust implies that these dilution factors have only a small influence on the observed amplitude, essentially compensating for their higher

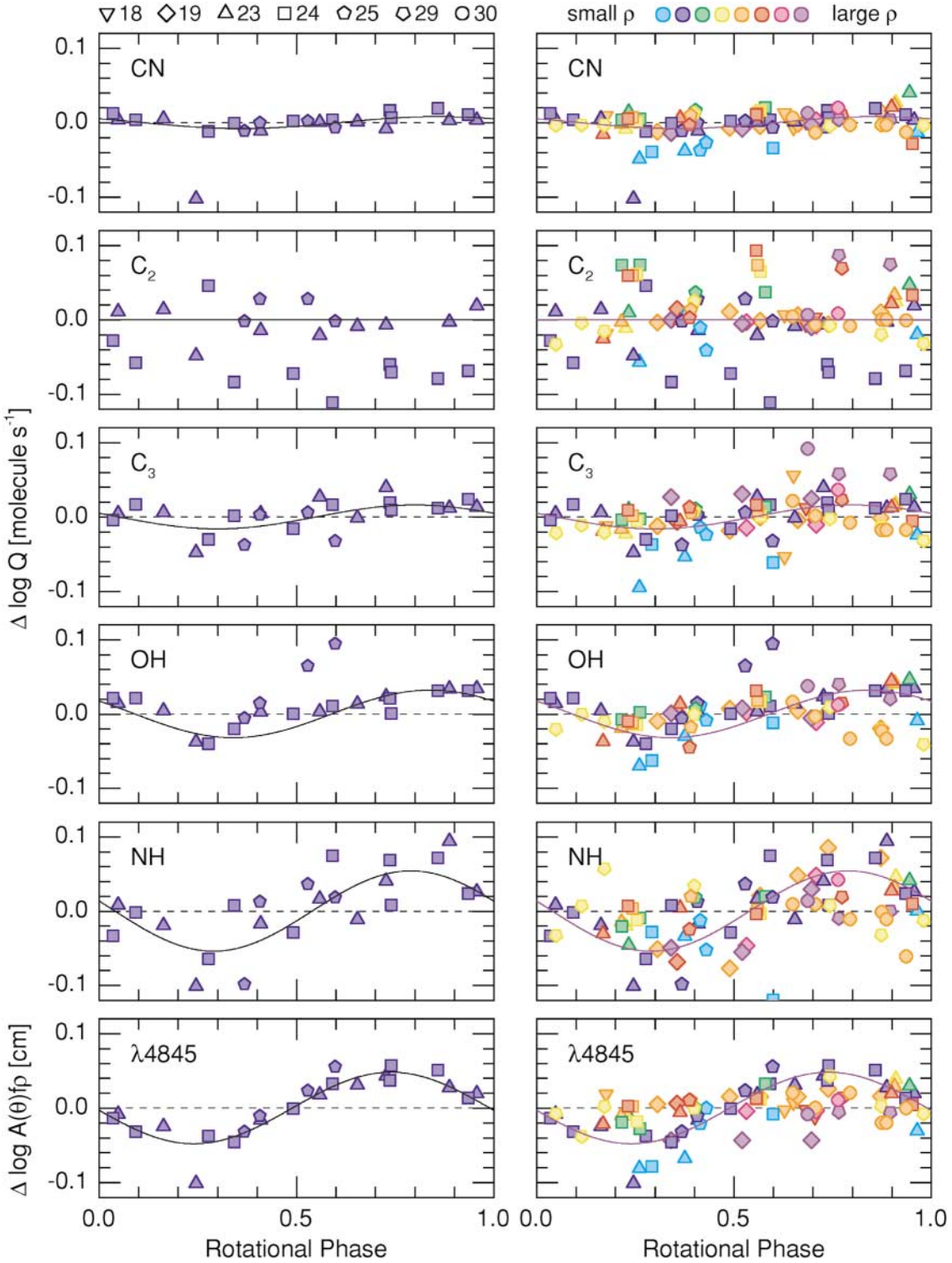

FIG. 5. Residual log of production rates for gas and dust plotted as a function of rotational phase, after removal of the outburst and correcting for aperture size (see Fig. 4), using our improved rotation period of 6.274 h. Colors vary with log ρ. In the left-hand column, only observations obtained with our monitoring aperture (27.5 arcsec) on March 23–25 are shown; the resulting projected aperture radius varied from 1200 to 1020 km. Note the clear rotational signature seen in OH, NH, and dust, as compared to the smaller amplitude displayed by C_3 and the nearly flat lightcurves of CN and C_2. In the right-hand column, all observations are shown from the interval March 18–30. Symbols again distinguish the different nights, as indicated in the key. As expected, larger aperture data show smaller amplitudes and phase shifts with respect to the monitoring aperture data; these effects greatly complicated the determination of the rotation period.

TABLE IV
Photometric Lightcurve[a] Monitoring Aperture Data for Comet Hyakutake (1996 B2)

Date (1996)	UT (hr)	ΔT[b] (day)	Rotational Phase[c]	log ρ (km)	$\Delta \log Q$ (molecule s^{-1}) OH	NH	CN	C_3	C_2	$\Delta \log A(\theta)f\rho$ (cm) UC	BC
Mar 23	5.98	–39.146	0.245	3.08	–0.038	–0.101	–0.102	–0.048	–0.048	–0.064	–0.101
Mar 23	7.01	–39.103	0.409	3.08	0.003	–0.017	–0.011	0.005	–0.015	–0.019	–0.016
Mar 23	7.93	–39.064	0.559	3.08	0.003	0.017	0.000	0.027	–0.021	0.005	0.018
Mar 23	8.54	–39.039	0.654	3.08	0.013	–0.011	0.001	–0.001	–0.009	0.038	0.031
Mar 23	8.99	–39.020	0.727	3.08	0.024	0.041	–0.008	0.040	–0.007	0.040	0.043
Mar 23	10.01	–38.978	0.888	3.08	0.034	0.094	0.003	0.012	–0.003	0.015	0.028
Mar 23	10.44	–38.960	0.956	3.08	0.034	0.026	0.004	0.013	0.019	0.027	0.020
Mar 23	11.01	–38.936	0.048	3.08	0.014	0.008	0.004	0.005	0.011	–0.001	–0.008
Mar 23	11.74	–38.906	0.163	3.08	0.004	–0.019	0.005	0.007	0.014	–0.028	–0.025
Mar 24	7.25	–38.092	0.277	3.02	–0.040	–0.064	–0.012	–0.030	0.046	–0.041	–0.037
Mar 24	7.67	–38.075	0.342	3.02	–0.020	0.008	–0.001	0.002	–0.083	–0.049	–0.045
Mar 24	8.60	–38.036	0.491	3.02	0.001	–0.028	0.002	–0.015	–0.072	0.007	–0.001
Mar 24	9.23	–38.010	0.591	3.02	0.011	0.074	0.004	0.017	–0.111	0.031	0.033
Mar 24	10.14	–37.972	0.736	3.02	0.021	0.069	0.017	0.020	–0.060	0.037	0.037
Mar 24	10.18	–37.971	0.740	3.02	0.001	0.009	0.007	0.010	–0.070	0.057	0.057
Mar 24	10.90	–37.940	0.858	3.02	0.031	0.072	0.019	0.012	–0.079	0.041	0.051
Mar 24	11.39	–37.920	0.935	3.02	0.031	0.024	0.011	0.024	–0.068	0.025	0.014
Mar 24	12.03	–37.894	0.034	3.02	0.022	–0.033	0.013	–0.004	–0.028	–0.012	–0.013
Mar 24	12.37	–37.879	0.092	3.02	0.022	–0.002	0.004	0.017	–0.057	–0.019	–0.031
Mar 25	2.65	–37.284	0.368	3.01	–0.006	–0.098	–0.011	–0.037	–0.002	–0.041	–0.032
Mar 25	2.91	–37.274	0.406	3.01	0.015	0.013	0.000	0.004	0.028	–0.009	–0.010
Mar 25	3.66	–37.242	0.529	3.01	0.065	0.037	0.002	0.006	0.028	0.026	0.024
Mar 25	4.09	–37.224	0.598	3.01	0.095	0.019	–0.006	–0.032	–0.002	0.079	0.056

[a] Differential log Q or log $A(\theta)f\rho$ after correction for aperture trends and removal of 2nd iteration outburst.
[b] Time from perihelion (1996 May 1.394).
[c] Rotational phase based on 0.26140 day period and zero point at perihelion.

outflow velocity of the gas. Furthermore, the variation of OH on March 25, as seen in $\Delta \log Q$, was considerably larger than the previous two nights at the same interval of rotational phase. Similar but less definitive increases in the relative amplitude as the outburst diminished with time are also seen for the dust and NH. These are consistent with the absolute rotational amplitude being constant with time, implying that the rotational variability was independent of the outburst. So why does NH display the largest amplitude? Even though NH is generally considered a granddaughter of NH_3, approximately 3% of NH is formed by the single-step dissociation of NH_3, based on photodissociation branching ratios (Huebner *et al.* 1992). While inefficient for the coma as a whole, we believe that the NH observed within the innermost coma was formed primarily by this dissociation path.

In comparison, the much reduced lightcurve amplitudes of CN, C_2, and, in particular, C_3, directly imply that a large amount of dilution must have occurred due to dilution by gas originating from outside of the aperture. Therefore, these carbon-bearing molecules must primarily arise from a distributed source, rather than directly from gas progenitors released from the nuclear active regions when the comet was at perigee. For CN and C_2, this is consistent with the observed aperture trends discussed in the previous section. In the case of C_3, however, this result is apparently in conflict with the flat trend with aperture size. This discrepancy may be due to differing proportions of C_3 arising from a distributed vs nuclear source as compared to CN and C_2, or simply due to the much shorter lifetime of C_3 limiting the range of any aperture trends. Unfortunately, the lack of small ρ measurements on nights other than March 23–25 prevents us from determining whether this was a characteristic of Hyakutake throughout the apparition, or whether this was primarily caused by material released by the outburst.

In the right-hand column of Fig. 5, we next look at all of observations in the time frame of March 18–30. Here we use colors to identify different projected aperture sizes, while continuing to distinguish different nights by symbol type. The monitoring aperture is shown in blue, while the smallest aperture measurements are in light blue and are systematically below the other data, as previously discussed. It is evident that larger aperture data (green, yellow, orange, red, magenta, and

violet) generally show progressively smaller amplitudes, especially for the dust. More difficult to see are trends in the position of the peak with aperture. The size and rate of change of these phase shifts differ from species-to-species for a combination of reasons. For instance, dust shows the expected increasing phase lag with increasing aperture size, along with the greatly diminishing amplitude. However, OH, NH, and C_3, show trends in the opposite direction, with the larger aperture (>2000 km) measurements in OH showing the lightcurve maximum leading in phase by as much as 0.3 of the monitoring aperture peak. This may be plausibly explained by the changing viewing geometry over the 13-day interval coupled with the outflow velocity of the gas blob/jet. For instance, if the jet were closer to the plane of the sky by late March, the projected velocity would be higher, and it would leave the aperture sooner, for any given projected aperture size. This scenario is also consistent with the generally smaller amplitudes observed for a given projected aperture size on March 18–19; the smaller amplitude would be due to the jets being more along the line of sight prior to perigee, and before one blob/jet left the aperture, the next one already began, flattening out the variability (Schleicher *et al.* 1998b). A detailed analysis of the time-dependent morphology in the various gas species will be treated in a subsequent paper focusing on our narrowband imaging data.

Rotation Period Determination

As mentioned briefly in the Introduction, the original analysis by Schleicher *et al.* (1998b) of the photometric lightcurve and imaging morphology of the dust in late March yielded a rotation period for Hyakutake of 6.23 ± 0.03 h (0.2596 ± 0.0013 day). However, a change in the period by even the quoted uncertainty of 0.03 h yields a phase shift of more than one-half cycle after just one month. In this section, we describe our successful efforts to refine the rotation period determination, so that various data sets obtained over a wider range of dates might be intercompared as a function of rotational phase.

Throughout our period analysis we employed the same methodology for the lightcurve analysis as was used by Schleicher *et al.* (1998b), where the best solution was determined using the phase dispersion minimization (PDM) technique combined with a careful "by eye" examination of the resulting phased lightcurves. This visual inspection allowed us to determine both a range of viable solutions (i.e., acceptable rotational phasing but with greater dispersion than the best solution) and a preferred answer utilizing information ignored by the PDM routine, such as aperture effects and possible night-to-night systematics due to the baseline and outburst removal.

Our initial efforts focused on supplementing the dust lightcurve with the inclusion of the OH, NH, and C_3 data from March 18–30 discussed in the previous section. Potential periods were investigated for each species separately, applying a variety of constraints on the projected aperture sizes. Unfortunately, a significant variation in the derived period resulted with these differing constraints. For instance, the smallest periods (0.256–0.257 days) were obtained for OH with $\log \rho < 3.5$, while the largest values (0.259–0.261 days) were measured for OH, NH, C_3, and the dust when the aperture size range was tightly restricted to minimize aperture effects. These restricted aperture results for the gas species confirmed, but did not improve upon, the original period determination.

We also attempted to apply additional leverage by means of a much larger time span, by including the observations from March 1—the only other night which exhibited a clear rotational signature. The four observational sets obtained with the same, large aperture ($\log \rho = 4.21$) spanned nearly 30% of a rotation cycle and showed a clear, increasing trend of the production rates. In this analysis, we were forced to restrict the late-March data to those obtained through relatively large apertures ($3.5 < \log \rho < 4.2$) and to apply an estimated phase shift of 0.10–0.15 to correct for the remaining aperture effects. This resulted in best periods of 0.2577, 0.2609, and 0.2642 days (each ± 0.0003, excluding uncertainties due to the assumed phase shift). The ambiguity among these three solutions is due to the long, 17-day gap in the observations, and not knowing a priori the number of rotational cycles between March 1 and March 18; however, the previous test results permit us to identify the intermediate solution as the correct solution.

Throughout these analyses it was clear that the effects of phase shifts were minimized when (1) aperture sizes were restricted to a small range of values, (2) the projected aperture size was small ($\log \rho < 3.3$), and (3) dust, rather than a gas species, was used. Fortunately, an additional photometric lightcurve matching these conditions was published by Lisse *et al.* (1999), from which they obtained a period of 6.3 ± 0.03 h. In their Fig. 7, they plot photometric aperture fluxes extracted from CCD observation obtained through IHW blue and red continuum filters on March 20, March 22, and March 23. For the extractions, they varied the aperture size in pixels to maintain a fixed projected aperture radius of 500 km. By combining data sets, we could significantly increase the total time span of small aperture dust observations.

Using their reduced fluxes as a starting point, we processed their measurements in a similar manner to our own. This involved first converting their aperture fluxes to $A(\theta) f \rho$ values; the resulting lightcurve and our own monitoring aperture data are shown in Fig. 6. As we discuss in the following section, the outburst clearly began just before their March 20 observations, during which the outburst is rapidly increasing in strength. By March 22, the outburst had already begun to decrease at a rate consistent with our March 23–25 data. Because both groups had nearly identical temporal coverage on March 23, the blue continuum measurements—both made with IHW 4845 Å filters—could be directly intercompared. An offset of 10% between the data sets is evident, an amount completely consistent with the expected aperture effect already discussed, given that their aperture radius of 500 km is significantly smaller than either our

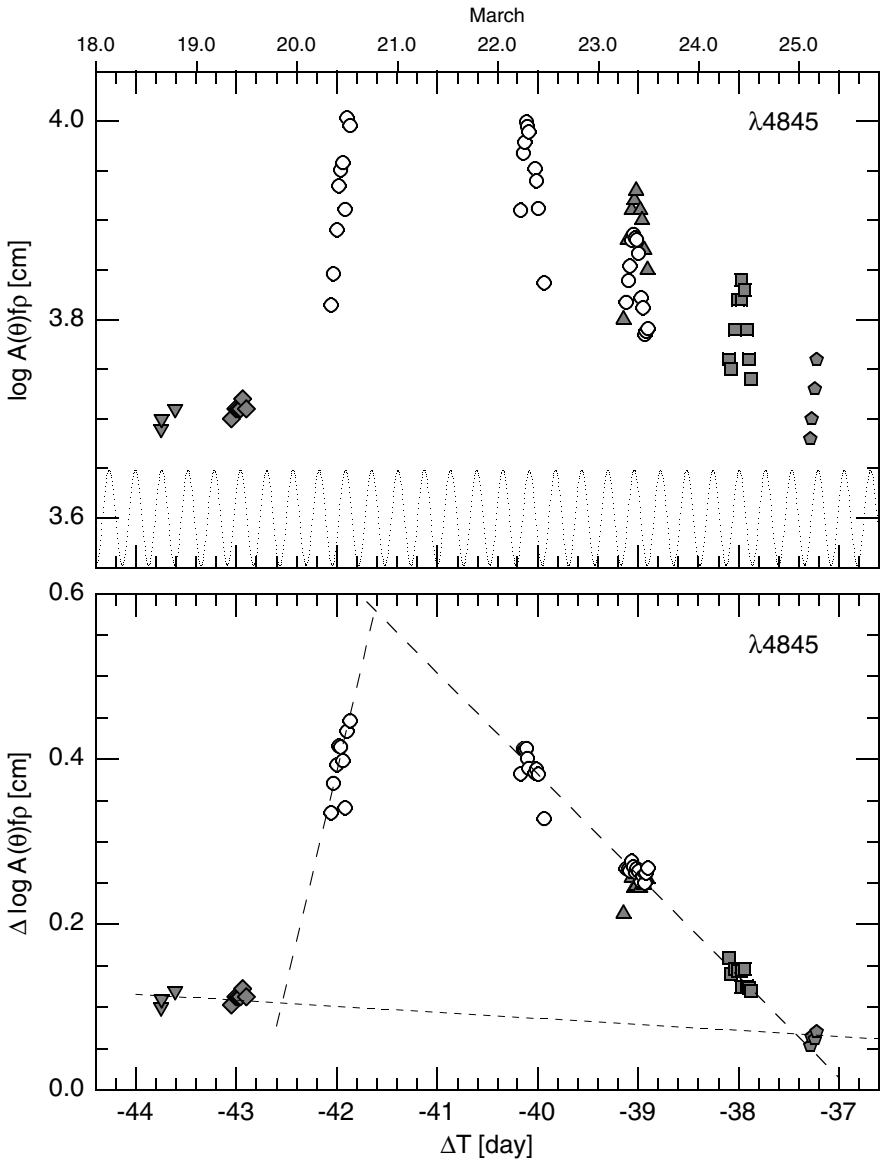

FIG. 6. Log $A(\theta)f\rho$ for the continuum at λ4845 plotted as a function of the time during the outburst in late March. Filled symbols are our measurements, either with the monitoring aperture on March 23–25 or a moderate-sized aperture ($3.40 < \log\rho < 3.55$) on March 18–19, while points based on fluxes in a small extraction aperture ($\log\rho = 2.70$) by Lisse *et al*. (1999) are presented as open circles. The top panel shows the good absolute agreement between the data sets on March 23, with the 10% offset being completely consistent with the expected aperture effects associated with small apertures (see Fig. 4). The rotational variability seen in Figs. 5 and 7 is represented by the sine curve. In the bottom panel, the r_H-dependent and aperture trends have been removed. In addition, rotational fits were removed from the Lisse *et al*. (1999) data, and from our monitoring aperture data, to show only the outburst. The much smaller rotational variability seen in the larger aperture data from March 18–19 was not removed. The local baseline is based on these March 18–19 data and on the March 29–30 data; note that the dust has returned to the baseline value by March 25. The onset time of the outburst is tightly confined, with a nominal date of March 19.85, based on the extrapolated linear fit to the rapidly rising measurements on March 20.

monitoring aperture (1200 km) or our smallest aperture (850 km) on this night.

We next removed the same r_H-dependence from their data as we used for our own blue continuum data and then applied the Lowess smoothing function with a span of 50% to remove the outburst. This last step conveniently also removed the overall offset due to aperture sizes. While this Lowess span worked well for March 22–23, it did not remove the strong upward trend on March 20. We, therefore, applied a simple iterative procedure for the removal of the upward trend on March 20. After fitting a sinusoid to the phased lightcurve from March 22 and March 23, we removed this rotational curve from the data for March 20 prior to the outburst removal. A least-squares fit to the "pure" outburst on March 20 was determined, and this linear fit was removed from the night of March 20 in the second iteration, to replace our original Lowess fit.

At this stage we could combine our monitoring aperture dust data with the processed data from Lisse *et al.* This required the application of a small but significant phase shift between the data sets to adjust for the phase trend with aperture size. The bulk of this shift could be readily determined by measuring the offset in time of lightcurve maximum in both data sets on March 23. This offset was almost exactly 0.5 h, corresponding to a phase shift of +0.08, and is comparable to the expected additional time of 0.57 h required for material to travel the additional 700 km to the edge of our aperture traveling at 0.34 km s^{-1} (Eberhardy *et al.* 2000). However, an additional small, negative adjustment was also necessary to compensate for the slight change in projected aperture sizes of our monitoring aperture from 1200 to 1020 km from March 23 to March 25. Testing a variety of rotational periods near our best solution from the Lisse *et al.* data, we could directly investigate small phase shifts in our own data between the three nights, ultimately concluding that a mean phase shift of 0.075 for our data with respect to the Lisse *et al.* data was best for these two data sets as a whole.

Applying this phase shift, we determined that the best value for the rotation period was 0.2614 ± 0.0003 days or 6.274 ± 0.007 h, where the quoted uncertainty includes the uncertainty in the phase shift between the data sets. In arriving at this solution, we deemphasized the data from March 20, due to the sharp but brief dip near maximum, and March 25, since neither a minimum nor a maximum was observed. We consider this solution for the period to be the most precise of our several attempts because it avoids the unknown uncertainties in aperture-induced phase shifts when the measurements from March 1 were utilized. The resulting phased lightcurve is shown in Fig. 7. We emphasize that our quoted result is the local synodic period, i.e., the length of a solar day on the nucleus, since it is the periodic release of material from the dominant active region which we measure, rather than brightness variations from the nucleus itself (which are completely overwhelmed by the dust coma). The corresponding sidereal period will be obtained as a component of the modeling of the dust jet morphology (Schleicher and Woodney 2002).

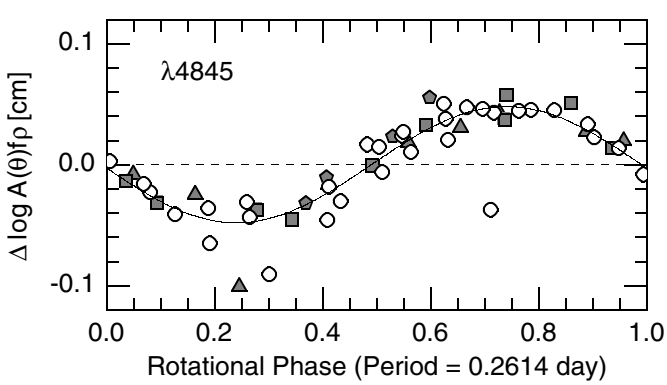

FIG. 7. Residual log $A(\theta)f\rho$ for λ4845 plotted as a function of rotational phase, after removal of the outburst and correcting for aperture size, using the combined data sets from Lisse *et al.* (1999) and our monitoring aperture. Symbols are the same as in Fig. 6. The Lisse *et al.* data have also had a phase shift of 0.075 applied, as discussed in the text, to adjust for aperture effects between the data sets. The rotational phasing is based on our final rotation period of 0.2614 ± 0.0003 day or 6.274 ± 0.007 h.

Outburst Characteristics

The final step in our overall iterative procedure was to use the rotation period and a sinusoidal approximation to the rotational lightcurve to remove the rotational variability, leaving only the outburst. We restricted this analysis to our monitoring aperture data from March 23–25, along with the dust data from Lisse *et al.*, to minimize complications due to aperture effects. To establish the nominal baseline for each species in late March, we also included some necessarily larger aperture data from March 18–19 and March 29–30. In these cases, we restricted ρ to the smallest aperture available and did not attempt to remove the muted rotational signature.

We first examine the outburst as detected in the dust, due to the improved temporal coverage provided by the combined data sets from Lisse *et al.* and ourselves. In Fig. 6, the top panel shows the outburst prior to the removal of the rotational lightcurve, along with the rotational sine curves. The bottom panel shows the outburst after the rotational variability has been removed separately from each data set, with appropriate changes in amplitude and the 0.075 phase shift discussed in the previous section. A rapid rise is clearly evident in the data from March 20, and a much slower, near-linear fall-off in $\Delta \log A(\theta) f\rho$ is seen from March 22–25, with the dust having reached the baseline on March 25; note that the local baseline on March 29–30 is at a value of 0.035, lower than the value of 0.11 on March 19. Linear least-squares fits have been determined for both the rise and fall portions of the outburst and these are also shown. Their intersection provides an approximate value and time for the peak, but we suspect that the actual outburst maximum was likely somewhat lower than the intersection but higher than the highest measured value, perhaps at $\Delta \log A(\theta) f\rho$ of 0.5, or about 3× the baseline dust production. The actual time of maximum can similarly be constrained to between ΔT of −41.8 and −41.2 days (March 20.6 and March 21.2), with the most likely time of −41.6 days (March 20.8).

The start time of the outburst can also be tightly constrained. First, the small increase visible in the March 19 data is consistent with the expected rotational variability, which was not removed from this larger aperture data. Therefore, given the lack of a significant change in dust production between March 18 and March 19, the outburst clearly began after these observations, i.e., after March 19.5 ($\Delta T = -42.9$). An absolute constraint is also imposed by the initial data points from March 20, at which time the outburst had already reached more than one-half of the peak value. The simple extrapolation of the linear fit (excluding the abnormally low point at rotation maximum; see Fig. 7) yields an intercept with the local baseline of $\Delta T = -42.55$ or March 19.85. A slight curvature in the data from March 20 is possible; if true, this would imply that the rate of increase was

steeper prior to these observations, and that the start-time was somewhat later, but prior to $\Delta T = -42.2$ or March 20.2.

These characteristics of the outburst can be used to constrain the nature of these new particles. While the relatively sharp peak might be explained by the source of the outburst abruptly turning off, the slow, steady recovery to the baseline level most likely implies that the peak represents the time when a significant fraction of the dust began reaching the edge of the aperture. In this scenario, the slow fall-off is caused by larger and larger particles (having lower and lower velocities) progressively leaving the aperture. The extreme of this size distribution is represented by the detection by several investigators of condensations moving down the tail in late March and early April. The first report by Lecacheux *et al.* (1996) noted "luminous knots" moving along the tail and that the inner part of the tail (<2000 km) had brightened significantly between March 21.2 and March 21.9. Knots were also measured by Desvoivres *et al.* (1999), and references therein, on numerous nights beginning March 22; Desvoivres *et al.* (2000) model the motion of seven fragments, each acting as a mini-nucleus producing a mini-coma, i.e., the observed condensations, and derive separation dates from March 20.3 to March 25.1. The largest and slowest moving of these only became distinct from the nuclear condensation on March 30, with a somewhat uncertain extrapolated separation date from the nucleus of March 21.4. Note that in all cases, the observed condensations produce an extremely small fraction of the total light of the overall outburst (Schleicher and Woodney 2002).

We suggest that the break-off of the largest fragment detected by Desvoivres *et al.* (2000) was the triggering event of the entire outburst and probably occurred simultaneously with or just prior to the start of the outburst recorded in the photometric record, i.e., ~March 19.85. The time from the onset of the outburst to maximum light, ~23 h, coupled with the aperture radius of 500 km, implies velocities of the faster moving dust grains of only ~6 m s^{-1}. Therefore, it is likely that these grains are largely produced by the successive fragmentation of larger, slow-moving grains. The rapid, large rise in the lightcurve implies that the fragmentation process also proceeded quickly, greatly increasing the total surface area of the dust.

Additional clues as to the nature of the outburst are provided by the relative behavior of the various gas species on March 23–25 as seen in Fig. 8 after aperture effects and rotational variability have been removed. In all cases, the apparent gas production was about 2× higher on March 23 than each species' local baseline production (which varied significantly from zero primarily due to the aperture adjustments made in the first iteration), as compared to the apparent dust production, which was about 1.6× higher than local baseline. Since all of the gas species have a similar outburst amplitude but differ from the dust, this might suggest different relative velocities between dust and gas. However, as noted earlier, CN, C_2, and C_3 essentially fall-off in a linear manner (in $\Delta \log Q$ vs ΔT), similar to but less steep than that of the dust. Their respective rates of decline, if continued, would reach local baselines 1–2 days after

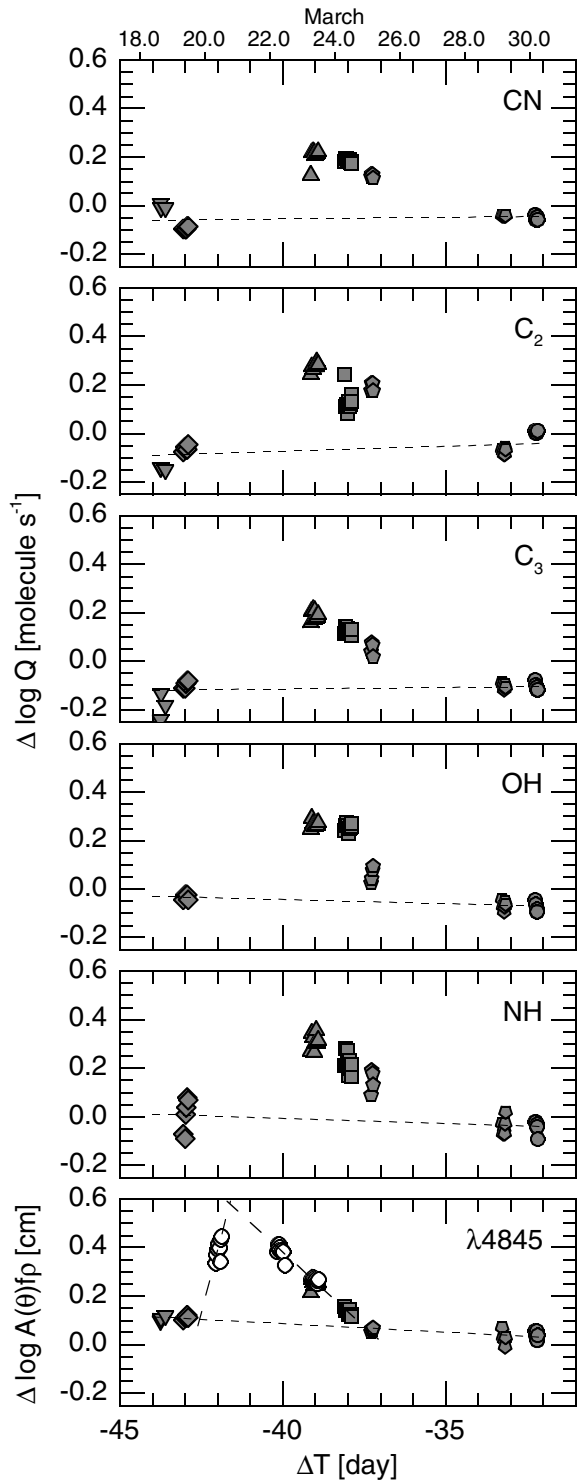

FIG. 8. Residual log production rates for gas species and the dust are shown as a function of time in late March. Similar to Fig. 6, the r_H-dependent and aperture trends have been removed, as well as the sinusoidal fits to the monitoring aperture data (shown in Fig. 5), to investigate the outburst characteristics for each species. Note the near-level behavior of OH on March 23 and March 24, followed by an abrupt drop on March 25 as compared to other species having steadier decreases with time. Also, the rate of recovery from the outburst of the carbon-bearing species appears to be slower than for OH, NH, or dust.

our observations on March 25. In comparison, OH maintains a near-constant level on March 23–24, but drops precipitously on March 25, almost completely returning to its baseline value, while NH again displays intermediate behavior between OH and the other species. A variety of scenarios may provide an explanation of these differences, but perhaps the simplest option is related to our proposed explanation of the small rotational amplitudes of the carbon-bearing species: That the majority of the CN, C_2, and C_3 measured within the photometer entrance aperture is originating outside of the aperture due to the time delay in the release of these gas molecules (or their parents) from their source, such as CHON particles, which are moving down the tail with time, yielding the gradual lightcurve decay. In contrast, the abrupt OH drop would have been caused by the water source moving out of the aperture. Backfilling of the aperture would be minimal for OH, and to a lesser extent, NH, simply if these species' parents are released much more rapidly from icy grains.

V. SUMMARY

Comet Hyakutake provided an excellent example of "the closer you look, the more you see." At a global scale, we find that the relative abundances of the minor gas species place Hyakutake into the "typical" category of comets in the A'Hearn *et al.* (1995) taxonomic classification system. A more precise value of the rotation period was obtained by utilizing only small aperture measurements to minimize phase lags and by extending the lightcurve with additional measurements by Lisse *et al.* (1999). This value, 0.2614 ± 0.0003 day, places Hyakutake squarely among the small number of comets with well-determined, rapid rotation rates. The spatial radial fall-off of OH was consistent with the expected nominal spatial distribution, while CN and C_2 displayed fall-offs more consistent with a distributed source (i.e., CHON grains), and the dust fall-off was significantly less steep than $1/\rho$, possibly due to fragmenting grains. Rotational lightcurve amplitudes were largest for OH, NH, and the dust, again consistent with the carbon-bearing species primarily originating from a distributed source. The heliocentric distance (r_H) dependence of the production rates of OH and NH were much shallower than those for either the carbon-bearing species or the visible dust. The derived water r_H-dependence was also significantly less steep than expected from a basic water vaporization model and required an effective active area varying from 29 km^2 at $r_H = 1.8$ AU to only 13 km^2 at 0.6 AU. If the possible contribution from icy grains is ignored, these active areas correspond to an effective active fraction varying from about 40 to 18%, based on independent estimates of the size of the nucleus. Alternatively, if icy grains are a significant source of water, they must release their water within approximately 1000 km of the nucleus and yield a progressively smaller fraction of the total water as the comet approached the Sun.

Revised reduction procedures were applied to the photometry to remove the C_3 contamination from the UV continuum filter, permitting dust colors to be extracted. The continuum spectrum was generally red, with the dust color progressively changing from being significantly reddened at large r_H to near-solar colors at small r_H. This change is most likely caused by a change in the particle size distribution. Focusing nearer to the time of closest approach, we find that a major outburst was initiated near March 19.9. The characteristic recovery from the outburst differed among the observed species, with dust and OH recovering most rapidly, essentially returning to baseline values by March 25. Our photometric analysis is consistent with this outburst being the initiator of the various fragments or condensations reported by other investigators.

A consistent overall picture emerges when we view these observational results as simple seasonal variations of a rotating heterogeneous nucleus of about 2.4-km radius, with one primary active region. The principle active area moves progressively into winter and out of sunlight during the pre-perihelion apparition. This naturally explains both the observed decrease in actively sublimating area as well as the change of dust color with heliocentric distance as the population of dust grains lifted from the active region makes up a shrinking fraction of the overall dust production. An alternative, self-consistent solution, would involve a near-nucleus population of icy grains which decreases as Hyakutake approached the Sun. These might be old, low velocity grains released early in the apparition, possibly from earlier outbursts, or a depleting supply of continuously released surface or subsurface grains, possibly fragmenting within the inner coma. A detailed analysis of our CCD imaging of dust in Hyakutake has recently been completed (Schleicher and Woodney 2002) investigating the detailed structure within the inner coma and implications about the embedded nucleus. The pole solution and source region locations determined from their Monte Carlo modeling of the coma morphology preclude any significant seasonal variation during the interval of photometric measurements discussed here. Therefore, of our two proposed scenarios, it appears that the icy grain scenario more accurately describes Comet Hyakutake's true behavior.

ACKNOWLEDGMENTS

We gratefully acknowledge the assistance of R. Millis, S. Lederer, and P. Birch in the acquisition of many of the reported observations, and L. Levy and S. Sackey for preliminary reductions. Y. Fernández and C. Lisse kindly provided their photometric fluxes in electronic form. We thank T. Farnham for numerous helpful discussions and for providing revised filter calibrations. This work was funded most recently by NASA Grants NAG5-9009 and NAG5-10444.

REFERENCES

A'Hearn, M. F. 1982. Spectroscopy and spectrophotometry of comets at optical wavelengths. In *Comets* (L. Wilkening, Ed.), pp. 433–460. Univ. of Arizona Press, Tucson.

A'Hearn, M. F., D. G. Schleicher, P. D. Feldman, R. L. Millis, and D. T. Thompson 1984. Comet Bowell 1980b. *Astron. J.* **89**, 579–591.

A'Hearn, M. F., P. V. Birch, P. D. Feldman, and R. L. Millis 1985. Comet Encke—Gas production and lightcurve. *Icarus* **64**, 1–10.

A'Hearn, M. F., R. L. Millis, D. G. Schleicher, D. J. Osip, and P. V. Birch 1995. The ensemble properties of comets: Results from narrowband photometry of 85 comets. *Icarus* **118**, 223–270.

Altenhoff, W. J., J. H. Bieging, B. Butler, H. M. Butner, R. Chini, C. G. T. Haslam, E. Kreysa, R. N. Martin, R. Mauersberger, J. McMullin, D. Muders, W. L. Peters, J. Schmidt, J. B. Schrami, A. Sievers, P. Stumpff, C. Thum, A. von Kap-herr, H. Wiesemeyer, J. E. Wink, and R. Zylka 1999. Coordinated radio continuum observations of Comets Hyakutake and Hale–Bopp from 22 to 860 GHz. *Astron. Astrophys.* **348**, 1020–1034.

Baum, W. A., T. J. Kreidl, and D. G. Schleicher 1992. Cometary grains. *Astron. J.* **104**, 1216–1225.

Bertaux, J. L., J. Costa, E. Quemerais, R. Lallement, M. Berthe, E. Kyrola, W. Schmidt, T. Summanen, T. Makinen, and C. Goukenleuque 1998. Lyman-α observations of Comet Hyakutake with SWAN on SOHO. *Planet. Space Sci.* **46**, 555–568.

Biver, N., D. Bockelée-Morvan, J. Crovisier, J. K. Davies, H. E. Matthews, J. E. Wink, H. Rauer, P. Colom, W. R. F. Dent, D. Despois, R. Moreno, G. Paubert, D. Jewitt, and M. Senay 1999. Spectroscopic monitoring of Comet C/1996 B2 (Hyakutake) with the JCMT and IRAM radio telescopes. *Astron. J.* **118**, 1850–1872.

Bockelée-Morvan, D., D. Gautier, D. C. Lis, K. Young, J. Keene, T. Phillips, T. Owen, J. Crovisier, P. F. Goldsmith, E. A. Bergin, D. Despois, and A. Wootten 1998. Deuterated water in Comet C/1996 B2 (Hyakutake) and its implications for the origin of comets. *Icarus* **133**, 147–162.

Brooke, T. Y., A. T. Tokunaga, H. A. Weaver, J. Crovisier, D. Bockelée-Morvan, and D. Crisp 1996. Near-infrared spectroscopy of molecules and radicals from Comet C/1996 B2 Hyakutake. *Bull. Am. Astron. Soc.* **28**, 1091.

Chernova, G. P., M. Ahmedzyanov, and N. N. Kiselev 1994. Photometry and polarimetry of Comet Shoemaker–Levy 1991a1. *Planet. Space Sci.* **42**, 623–625.

Cleveland, W. S. 1979. Robust locally weighted regression and smoothing scatterplots. *J. Am. Stat. Assoc.* **74**, 829–836.

Cochran, A. L., and D. G. Schleicher 1992. Observational constraints on the lifetime of cometary H_2O. *Icarus* **105**, 235–253.

Cowan, J. J., and M. F. A'Hearn 1979. Vaporization of cometary nuclei: Light curves and lifetimes. *Moon Planets* **21**, 155–171.

de Pater, I., J. R. Forster, M. Wright, B. J. Butler, P. Palmer, J. M. Veal, M. F. A'Hearn, and L. E. Snyder 1998. BIMA and VLA observations of Comet Hale–Bopp at 22–115 GHz. *Astron. J.* **116**, 987–996.

Desvoivres, E., J. Klinger, A. C. Levasseur-Regourd, J. Lecacheux, L. Jorda, A. Enzian, F. Colas, E. Frappa, and P. Laques 1999. Comet C/1996 B2 Hyakutake: Observations, interpretation and modelling of the dynamics of fragments of cometary nuclei. *Mon. Not. R. Astron. Soc.* **303**, 826–834.

Desvoivres, E., J. Klinger, A. C. Levasseur-Regourd, and G. H. Jones 2000. Modeling the dynamics of cometary fragments: Application to Comet C/1996 B2 Hyakutake. *Icarus* **144**, 172–181.

Dutrey, A., D. Despois, D. Bockelée-Morvan, P. Colom, N. Biver, J. Crovisier, E. Gérard, H. Rauer, M. Grewing, S. Guilloteau, R. Lucas, R. Neri, and J. Wink 1996. Comet C/1996 B2 (Hyakutake). *IAU Circ.*, No. 6364.

Eberhardy, C. A., L. M. Woodney, and D. G. Schleicher 2000. Gas and dust jet morphology as a function of rotation in Comet Hyakutake (1996 B2) at perigee. *Bull. Am. Astron. Soc.* **32**, 1072–1073.

Farnham, T. L., D. G. Schleicher, and M. F. A'Hearn 2000. The HB narrowband comet filters: Standard stars and calibrations. *Icarus* **147**, 180–204.

Fernández, Y. R., A. Kundu, C. M. Lisse, and M. F. A'Hearn 1997. X-Band VLA* observations of Comet Hyakutake (C/1996 B2) and implications for nuclear properties. *Planet. Space Sci.* **45**, 735–739.

Greenberg, J. M., and B. A. S. Gustafson 1981. A comet fragment model for zodiacal light particles. *Astron. Astrophys.* **93**, 35–42.

Gustafson, B., and L. Kolokolova 1999. A systematic study of light scattering by aggregate particles using the microwave analog technique: Angular and wavelength dependence of intensity and polarization. *J. Geophys. Res.* **104**, 31,711–31,720.

Hanner, M. S., and R. L. Newburn 1989. Infrared photometry of Comet Wilson (19861) at two epochs. *Astron. J.* **97**, 254–261.

Harmon, J. K., S. J. Ostro, L. A. M. Benner, K. D. Rosema, R. F. Jurgens, R. Winkler, D. K. Yeomans, D. Choate, R. Cormier, J. D. Giorgini, D. L. Mitchell, P. W. Chodas, R. Rose, D. Kelley, M. A. Slade, and M. L. Thomas 1997. Radar detection of the nucleus and coma of Comet Hyakutake (C/1996 B2). *Science* **278**, 1921–1924.

Harris, W. M., M. R. Combi, R. K. Honeycutt, and B. E. A. Mueller 1997. Evidence for interacting gas flows and an extended volatile source distribution in the coma of Comet C/1996 B2 (Hyakutake). *Science* **277**, 676–681.

Haser, L. 1957. Distribution d'intensite dans la tete d'une comete. *Bull. Acad. R. Belgique, Classes des Sci.* **43**, 740–750.

Hicks, M. D., and U. Fink 1997. Spectrophotometry and development of emissions for C/1996 B2 (Hyakutake). *Icarus* **127**, 307–318.

Huebner, W. F., J. J. Keady, and S. P. Lyon 1992. Solar photo rates for planetary atmospheres and atmospheric pollutants—Solar flux. *Astrophys. Space Sci.* **195**, 1–294.

Jewitt, D. C., and H. E. Matthews 1997. Submillimeter continuum observations of Comet Hyakutake (1996 B2). *Astron. J.* **113**, 1145–1151.

Joshi, U. C., K. S. Baliyan, S. Ganesh, A. Chitre, H. O. Vats, and M. R. Deshpande 1997. A polarization study of Comet Hyakutake (C/1996 B2). *Astron. Astrophys.* **319**, 694–698.

Kiselev, N. N., and F. P. Velichko 1998. Polarimetry and photometry of Comet C/1996 B2 Hyakutake. *Icarus* **133**, 286–292.

Kissel, J., D. E. Brownlee, K. Bucher, B. C. Clark, H. Fechtig, E. Grun, K. Hornung, E. B. Igenbergs, E. K. Jessberger, F. R. Krueger, H. Kuczera, J. A. M. McDonnell, G. M. Morfill, J. Rahe, G. H. Schwehm, Z. Sekanina, N. G. Utterback, H. J. Volk, and H. A. Zook 1986. Composition of Comet Halley dust particles from Giotto observations. *Nature* **321**, 336–337.

Kolokolova, L., K. Jockers, G. Chernova, and N. Kiselev 1997. Properties of cometary dust from color and polarization. *Icarus* **126**, 351–361.

Kolokolova, L., K. Jockers, B. Gustafson, and G. Lichtenberg 2001. Color and polarization as indicators of comet dust properties and evolution in the near-nucleus coma. *J. Geophys. Res.* **106**, 10,113–10,128.

Laffont, C., P. Rousselot, J. Caliremidi, and G. Moreels 1998. Condensations and diffuse source of C_2 in Comet Hyakutake C/1996 B2. *Planet. Space Sci.* **46**, 585–601.

Lecacheux, J., L. Jorda, A. Enzian, J. Klinger, F. Colas, E. Frappa, and P. Laques 1996. Comet C/1996 B2 Hyakutake. *IAU Circ.*, No. 6354.

Lis, D. C., J. Keene, K. Young, T. G. Phillips, D. Bockelée-Morvan, J. Crovisier, P. Schilke, P. F. Goldsmith, and E. A. Bergin 1997. Spectroscopic observations of Comet C/1996 B2 (Hyakutake) with the Caltech submillimeter observatory. *Icarus* **130**, 355–372.

Lisse, C., M. Mumma, R. Petre, K. Dennerl, J. Schmitt, J. Englhauser, and J. Truemper 1996. Comet C/1996 B2 (Hyakutake). *IAU Circ.*, No. 6373.

Lisse, C. M., Y. R. Fernández, A. Kundu, M. F. A'Hearn, A. Dayal, L. K. Deutsch, G. G. Fazio, J. L. Hora, and W. F. Hoffmann 1999. The nucleus of Comet Hyakutake (C/1996 B2). *Icarus* **140**, 189–204.

Manset, N., and P. Bastien 2000. Polarimetric observations of Comets C/1995 O1 Hale–Bopp and C/1996 B2 Hyakutake. *Icarus* **145**, 203–219.

Matthews, H. E., N. Biver, M. Senay, J. K. Davies, W. R. F. Dent, D. Bockelée-Morvan, D. Jewitt, T. Owen, J. Crovisier, H. Rauer, and D. Gautier 1996. Comet C/1996 B2 (Hyakutake). *IAU Circ.*, No. 6353.

Millis, R. L., and D. G. Schleicher 1986. Rotational period of Comet Halley. *Science* **324**, 646–649.

Mumma, M. J., M. A. Disanti, M. Fomenkova, K. Magee-Sauer, N. R. dello Russo, and D. X. Xie 1996. Discovery of abundant ethane and methane in C/1996 B2 Hyakutake: Implications for cometary and interstellar organic chemistry. *Bull. Am. Astron. Soc.* **28**, 1090–1091.

Osip, D. J., D. G. Schleicher, and R. L. Millis 1992. Comets—Groundbased observations of spacecraft mission candidates. *Icarus* **98**, 115–124.

Rousselot, P., C. Arpigny, H. Rauer, A. L. Cochran, R. Gredel, W. D. Cochran, J. Manfroid, and A. Fitzsimmons 2001. A. fluorescence model of the C_3 radical in comets. *Astron. Astrophys.* **368**, 689–699.

Sarmecanic, J., M. Fomenkova, and B. Jones 1996. Mid-infrared imaging of C/1996 B2 (Hyakutake). *Bull. Am. Astron. Soc.* **28**, 1089.

Schleicher, D. G. 1996. Comet C/1996 B2 (Hyakutake). *IAU Circ.*, No. 6311.

Schleicher, D. G., R. L. Millis, D. T. Thompson, P. V. Birch, R. Martin, D. J. Tholen, J. R. Piscitelli, N. L. Lark, and H. B. Hammel 1990. Periodic variations in the activity of Comet P/Halley during the 1985/1986 apparition. *Astron. J.* **100**, 896–912.

Schleicher, D. G., R. L. Millis, D. J. Osip, and P. V. Birch 1991. Comet Levy (1990c)—Groundbased photometric results. *Icarus* **94**, 511–523.

Schleicher, D. G., R. L. Millis, and P. V. Birch 1998a. Narrowband photometry of Comet P/Halley: Variation with heliocentric distance, season, and solar phase angle. *Icarus* **132**, 397–417.

Schleicher, D. G., R. L. Millis, D. J. Osip, and S. M. Lederer 1998b. Activity and rotation period of Comet Hyakutake (1996 B2). *Icarus* **131**, 233–244.

Schleicher, D. G., and L. M. Woodney 2002. Analyses of dust coma morphology of Comet Hyakutake (1996 B2) near perigee: Outburst behavior, jet motion, source region locations, and nucleus pole orientation. *Icarus*, submitted.

Woodney, L. M., J. McMullin, and M. F. A'Hearn 1997. Detection of OCS in Comet Hyakutake (C/1996 B2). *Planet. Space Sci.* **45**, 717–719.